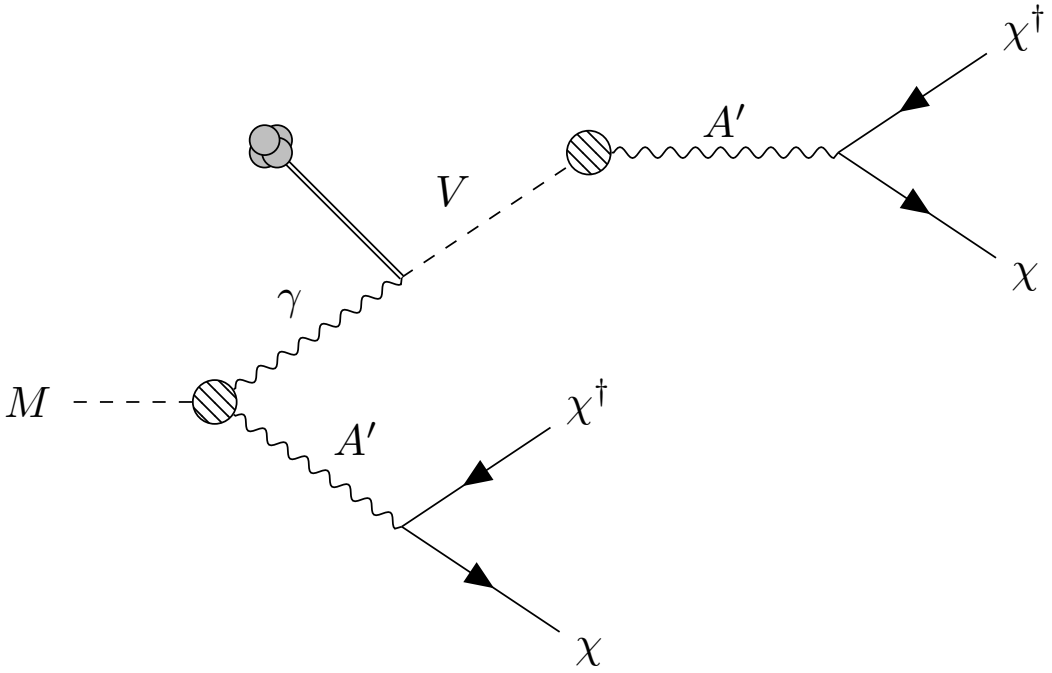

Sensitivity of Proton Fixed-Target Experiments to Light Dark Matter

Primary and Secondary Production Channels

Master's thesis in Physics

ALBIN LEDELL

DEPARTMENT OF PHYSICS AND ASTRONOMY

CHALMERS UNIVERSITY OF TECHNOLOGY
Gothenburg, Sweden 2026
www.chalmers.se

Master's thesis 2026

Sensitivity of Proton Fixed-Target Experiments to Light Dark Matter

Primary and Secondary Production Channels

Albin Ledell

CHALMERS
UNIVERSITY OF TECHNOLOGY

Department of Physics and Astronomy
Division of Subatomic, High-Energy and Plasma Physics
Theoretical Subatomic Physics
Chalmers University of Technology
Gothenburg, Sweden 2026

Sensitivity of Proton Fixed-Target Experiments to Light Dark Matter:
Primary and Secondary Production Channels

Albin Ledell

Supervisor: Riccardo Catena & Taylor Gray, Department of Physics and Astronomy
Examiner: Riccardo Catena, Department of Physics and Astronomy

Master's Thesis 2026
Department of Physics and Astronomy
Division of Subatomic, High-Energy and Plasma Physics
Theoretical Subatomic Physics
Chalmers University of Technology
SE-412 96 Gothenburg
Telephone: +46 31 772 1000

Cover: Schematic illustration of the secondary invisible vector meson (IVM) production channel considered in this thesis. An ordinary photon, produced through meson decay, converts to a vector meson via photoproduction in the presence of a nucleus, which subsequently decays into dark matter through kinematic mixing. One of the primary production channels, dark meson decay, is also depicted.

Typeset in LaTeX
Printed by Chalmers Digital Printing
Gothenburg, Sweden 2026

Sensitivity of Proton Fixed-Target Experiments to Light Dark Matter:
Primary and Secondary Production Channels

Albin Ledell
Department of Physics and Astronomy
Chalmers University of Technology

Abstract

Despite its remarkable success, the Standard Model of particle physics falls short of being a completely satisfactory theory. One prominent shortcoming is its inability to account for all the matter in the Universe, a discrepancy best explained by the presence of dark matter. Astrophysical and cosmological observations strongly indicate its existence, yet no non-gravitational interactions have been observed. The persistent null result may be attributed to dark matter being lighter than previously hypothesised, allowing it to have gone unnoticed in previous searches. This has driven growing interest in accelerator-based experiments, particularly fixed-target experiments. In this thesis, light dark matter (LDM) is investigated at proton fixed-target experiments, focusing on a minimal dark sector model with complex scalar dark matter and a dark vector mediator. Using the MadDump plugin to the MadGraph5_aMC@NLO framework, the sensitivity of the primary dark matter production channels is studied for the forthcoming experiments SHiP and DUNE ND, as well as the operational NOνA ND. In particular, the newly approved SHiP design and different operational modes of DUNE ND are considered. Additionally, a new secondary production channel in the form of photoproduced vector meson decay is considered, with the analysis performed largely analytically. This channel has recently been shown to enhance sensitivity in electron beam experiments. Here, no such enhancement is observed. The origin of this difference is not yet fully understood, with possible explanations including an insufficient flux of high-energy photons in the processes considered and a potential overestimation of dark photon production in the primary channel.

Keywords: Light Dark Matter (LDM), Dark Photon (DP), Proton Beam Experiment, Photoproduction, SHiP, DUNE ND, NOνA ND, MadDump, Beyond the Standard Model (BSM).

Acknowledgements

First and foremost, I would like to express my sincere gratitude to my supervisor and examiner Prof. Riccardo Catena for the opportunity to explore one of the most interesting frontiers of particle physics, as well as for the guidance and support throughout the project. Secondly, I would like to extend my deepest gratitude to my second supervisor, Taylor Gray. Our discussions and your willingness to take the time to address my many questions along the way have been invaluable in completing the thesis.

Furthermore, I would like to thank everyone in the office for enjoyable conversations and support. Thank you to all the PhD students at the Division of Subatomic, High Energy and Plasma Physics for inviting us to participate in the journal club, which has expanded my understanding of physics and led to many engaging discussions about the nature of reality.

To my friends and family, thank you for your support and for reminding me to sometimes let go of the work and enjoy more than just physics. To my dear Roxanne, your love and encouragement mean everything to me.

Albin Ledell, Gothenburg, June 2026

List of Acronyms

BBN	Big Bang Nucleosynthesis
BSM	Beyond the Standard Model
CDF	Cumulative Distribution Function
CDM	Cold Dark Matter
CL	Confidence Level
CMB	Cosmic Microwave Background
DIS	Deep Inelastic Scattering
DM	Dark Matter
DUNE	Deep Underground Neutrino Experiment
FD	Far Detector
HDM	Hot Dark Matter
IVM	Invisible Vector Meson
LAr	Liquid Argon
LDM	Light Dark Matter
LSS	Large-Scale Structure
MACHO	Massive Astrophysical Compact Halo Objects
MOND	MOdified Newtonian Dynamics
ND	Near Detector
NOνA	NuMI Off-Axis ν_e Appearance Experiment
PBH	Primordial Black Hole
PDF	Parton Distribution Function
POT	Protons On Target
PRISM	Precision Reaction-Independent Spectrum Measurement
QCD	Quantum Chromodynamics
QFT	Quantum Field Theory
(R)AQUAL	(Relativistic) AQUAdratic Lagrangian
SHiP	Search for Hidden Particles
SM	Standard Model
SND	Scattering and Neutrino Detector
SPS	Super Proton Synchrotron
TeVeS	Tensor-Vector-Scalar
UFO	Universal FeynRules Output
WIMP	Weakly Interacting Massive Particle
WISP	Weakly Interacting Slim Particles

Table of contents

List of figures

List of tables

1

Introduction

The development of particle physics, which took place mostly during the 20th century, has been one of the major achievements in physics. It stretches from Thomson's discovery of the electron in 1897 [1], to the atomic model by Rutherford (1911) [2] and Bohr (1912) [3], to the development of quantum mechanics by Heisenberg and Schrödinger, and finally culminating in the Standard Model (SM) as we know it today—governed by three gauge symmetries and involving quarks, leptons, gauge bosons, and the Higgs boson [4]. In fact, the final missing piece of the Standard Model, the Higgs boson, was not discovered until 2012 [5]. Despite its great predictive power, the Standard Model falls short of being a complete theory. It excludes gravity, which remains best described by Einstein's theory of general relativity, and it makes no predictions at higher energy scales [4], suggesting the existence of a more fundamental theory. It also carries some unsatisfactory features, for example, only partially unifying the gauge symmetries and exhibiting a hierarchy problem.

The Standard Model also seemingly fails in another important respect, namely accounting for all the matter in the universe [6]. Astrophysical and cosmological observations reveal that only about 16% of the matter content of the universe is baryonic, leaving roughly 84% unaccounted for. This implies the presence of matter that interacts predominantly through gravity whilst interacting only feebly otherwise. In the literature, this is referred to as dark matter (DM). Its nature remains a mystery to this day, giving rise to an exciting frontier of discovery.

All current evidence for dark matter merely being gravitational in nature leads to considerable uncertainty regarding not only its properties, but also its existence [6]. A key challenge of particle physics is consequently to characterise these properties. One detection method that has attracted particular recent interest is fixed-target experiments, where a high-energy beam is directed toward a stationary target [7]. This is especially motivated by a growing shift of interest towards so-called light dark matter (LDM) candidates, following unsuccessful searches for dark matter at higher mass. LDM is largely insensitive to historically popular search methods, such as direct detection experiments relying on dark matter present in our Galaxy. Producing LDM in a controlled fixed-target environment, where detection of such light particles is feasible, therefore presents a promising avenue. Whilst electron beam experiments are also of great interest, proton beam experiments offer an alternative route. Although

plagued by less sensitive detection methods, they compensate with greater beam power and additional production channels. Interest in dark matter searches using proton beam experiments is further driven by new experiments currently under development, including SHiP and DUNE, as well as existing experiments such as NOνA.

Proton beam experiments are therefore a subject of considerable interest. This thesis serves as a status report on the three aforementioned experiments, as well as an updated study of their sensitivity to the primary dark matter production channels. In particular, SHiP has recently undergone a design update, and the two configurations are compared. DUNE is primarily a neutrino experiment but may also be used to search for LDM, and may operate in different modes, each of which is compared. In addition to the primary channels, a new secondary production channel is considered at proton beam experiments, motivated by a recent paper by Schuster et al. [8] demonstrating increased sensitivity when including this channel at electron beam experiments. Whilst one of the primary channels at proton beam experiments involves direct meson production in the collisions, followed by decay to dark matter, this new channel considers vector mesons produced secondarily through photon conversion in the presence of a nucleus—an exclusive photoproduction process—which then may decay to dark matter. Despite its inclusion of primary meson decay, proton beams enables more photon production channels, photons which can convert to secondary vector mesons via photoproduction, making it plausible that a similar sensitivity enhancement could occur. The motivation for this thesis is hence twofold: an updated sensitivity study of the primary production channels at three benchmark proton beam fixed-target experiments, and an investigation of this new complementary production channel.

The thesis is organised as follows. Chapter 2 provides the basic background for the thesis, including the experimental evidence for the presence of dark matter, its basic properties, candidates, and production mechanism. A brief overview of the different dark matter searches is also presented. The specific dark matter model considered in this thesis is then outlined, followed by a recap of meson physics. Chapter 3 concerns the main analysis of proton beam experiments. It contrasts them with electron beam experiments, gives an overview of the three aforementioned experiments, and reviews the primary production channels and detection strategies. Chapter 3 then concludes with a presentation of the simulation tools used to study the sensitivity, as well as discussion on the statistical analysis performed to obtain the exclusions plots. Chapter 4 focuses on the new secondary production channel, presenting the computation of its sensitivity, largely performed analytically, from beam collision to detection. The results of these last two chapters are presented and discussed in Chapter 5. Chapter 6 provides the conclusions of the thesis.

Throughout this thesis, natural units $c = \hbar = 1$ are adopted. Consequently, all energies and masses are given in units of eV unless stated otherwise. Following the convention of particle physics, the mostly-minus signature $\eta_{\mu\nu} = \text{diag}(+1, -1, -1, -1)$ is used.

2

Background

Before the analyses, a background introducing the relevant subjects and concepts is in order. For readers unfamiliar with dark matter, this chapter begins by presenting some of the evidence, properties, proposed origins, and search strategies for dark matter. This is followed by a more formal introduction to the specific dark matter model adopted in this thesis. The chapter concludes with a brief review of mesons, motivated by their significance to the analysis.

2.1 The Case for Dark Matter

Although dark matter remains a great mystery, there is considerable evidence for its existence, not all of which can be covered here. Instead, this section is restricted to a fraction of the most prominent ones, described briefly with the intention of conveying only the basic principles. Importantly, all confirmed evidence rely exclusively on gravitational interactions [6], and those presented here are no exception. Spanning different length scales, the evidence is presented in three categories of increasing scale: galactic, cluster, and cosmological.

2.1.1 Galactic-Scale Evidence

Spiral galaxies are disc-shaped systems with spiral arms, rotating about their vertical axis, with most of their visible mass concentrated either in the dense central bulge or in the arms far from the centre [6]. By measuring the Doppler shift of atomic lines from stars and hydrogen clouds in the arms, the circular velocity as a function of distance from the galactic centre, $v(r)$, can be obtained. These are known as rotation curves. Applying Newtonian mechanics yields

$$m\frac{v^2}{r} = \frac{GM(r)m}{r^2} \implies v(r) = \sqrt{\frac{GM(r)}{r}}. \tag{2.1}$$

Given the mass distribution of the spiral galaxy, far away from the galactic centre the visible mass is approximately enclosed within the orbit, $M(r) \approx M$ is roughly constant, and the circular velocity is therefore expected to follow a Keplerian decline $v(r) \propto r^{-1/2}$.

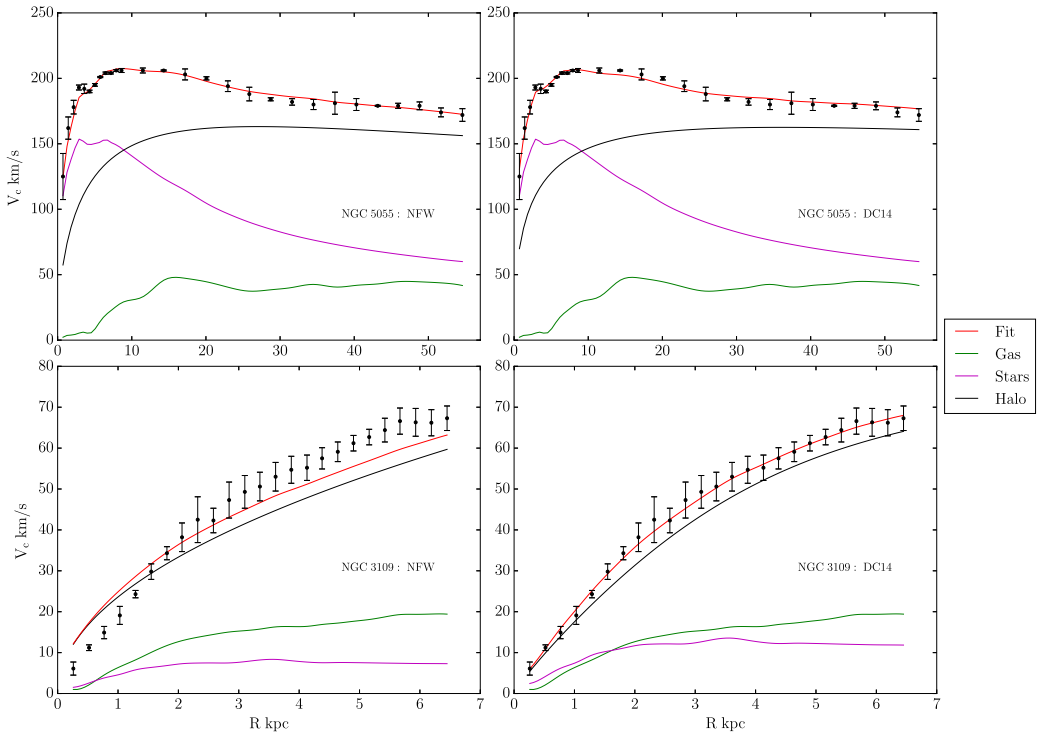

Figure 2.1: Rotation curves from [9], showing the rotational velocity as a function of distance from galactic centre. Green and pink lines correspond to gas and stellar contributions, respectively. Upper (lower) panels contain high-mass (low-mass) galaxies, left (right) panels contain the best dark matter fit using NFW (DC14) method, shown as the black line. In all four cases, the red line represents the combined contribution from the observed gas and stars, together with the fitted dark matter contribution. The approximately flat observed rotation curves are well described by the inclusion of a dark matter component.

Nevertheless, observational data reveal a flat rotation curve, $v(r) = \text{const}$, far from the galactic centre rather than the Keplerian decline (see figure 2.1). The observed circular velocities are too high; under such conditions, the peripheral stars should escape and the galaxy form would dissolve [6]. This discrepancy is resolved by the presence of additional invisible matter, explaining the form of the rotation curve. This is precisely dark matter. Assuming spherical symmetry, dark matter could take the form of a halo with mass density $\rho \propto r^{-2}$, such that $M(r) \propto r$. Substituting this into equation (2.1) yields a constant rotation curve. Whilst this is a simplified illustration, more rigorous models arrive at consistent results, indicating the necessity of dark matter.

2.1.2 Cluster-Scale Evidence

Galaxy clusters are the largest gravitationally bound systems in the universe, containing hundreds to thousands of galaxies [6]. Using the virial theorem

$$2\langle K\rangle + \langle V\rangle = 0, \tag{2.2}$$

relating the average kinetic energy to the average gravitational potential energy, Zwicky [10] argued as early as 1937 that the total mass of the Coma cluster exceeded its observed visible mass, thereby indicating the presence of dark matter needed to keep the cluster gravitationally bound. Whilst not fully accepted at the time, X-ray observations since the 1980s have employed similar but more sophisticated methods on a microscopic scale [6]. Rather than inferring kinetic energy from the velocity dispersion of galaxies, the temperature of the gas molecules is used to determine the total gravitational mass required to keep the cluster bound, once again implying the presence of dark matter.

In 2006, a pair of colliding clusters now known as the Bullet cluster was discovered [6]. Its distribution of baryonic matter can be traced by X-ray emissions, whilst the total mass, comprising both visible and dark matter, can be inferred independently through weak lensing. Lensing refers to the bending of light by matter according to general relativity, with "weak" referring to the regime where this bending is small (not strong enough for creating multiple images or an arc). Using these methods, a striking result emerged: the distributions of visible and dark matter are spatially separated.

A natural interpretation follows. Before the collision, each cluster contained an ordinary mix of visible and dark matter [6]. Upon colliding, the visible matter interacted with itself, causing the hot gas in each cluster to experience shock waves. On the contrary, dark matter interacts negligibly and therefore simply passed through, producing the observed separation. Since then, multiple similar systems have been found exhibiting the same behaviour. This type of evidence is not only indicative of dark matter, but is also hard to reconcile with alternative theories, such as modified gravity theories.

2.1.3 Cosmological-Scale Evidence

The present uniform expansion of the Universe suggests that it may have emerged from a past singular state characterised by infinite density [11]. Whilst our current laws of physics break down at this point, what followed was a rapid expansion known as the Big Bang. The early universe was radiation-dominated, filled with high-energy relativistic photons and neutrinos. Through pair production and similar processes, elementary particles such as quarks and leptons were produced, which subsequently formed hadrons. Eventually, the Universe cooled sufficiently to enter a period known as Big Bang nucleosynthesis (BBN), during which light atomic nuclei formed. Later still, the Universe became matter-dominated and ultimately cooled enough for electrons to combine with nuclei, forming the first neutral atoms.

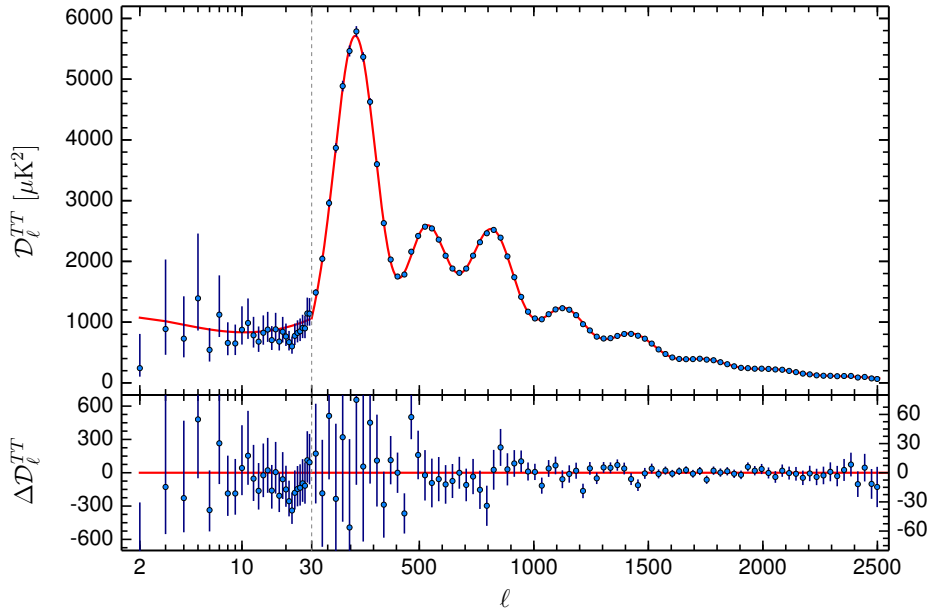

Figure 2.2: The CMB power spectrum from [12]. Blue dots are measured values of the CMB power spectrum with 1σ error bars and the red line is the theoretical prediction. Upper (lower) panels shows the spectrum (residuals between spectrum fit and measurement). Note that the horizontal axis changes from logarithmic to linear scaling at $l = 30$, as indicated by the vertical dashed line.

Before this epoch of atom formation, known as recombination, radiation interacted with matter primarily through Thomson scattering [11]. Photons could not travel freely, instead scattering repeatedly and essentially coupling strongly with the baryonic matter to form a single matter fluid. After recombination, the vast majority of electrons became bound to nuclei, rendering Thomson scattering negligible and making the Universe transparent for the first time. The remnant photons from this epoch still traverse the Universe today and are known as the Cosmic Microwave Background (CMB).

The tightly coupled baryon-photon fluid prior to recombination had a large relativistic sound speed, causing pressure to dominate over gravitational collapse, thereby preventing clustering [6]. Instead, the fluid experienced damped oscillatory behaviour in the form of pressure waves, known as baryonic acoustic oscillations. Clustering of baryonic matter could therefore only begin after recombination. According to the standard cosmological model, the early Universe was almost perfectly smooth, with only tiny inhomogeneities generated during inflation. This smoothness is confirmed by the CMB. A universe with only baryonic matter would consequently have been unable to develop the large inhomogeneities and rich large-scale structures (LSS) observed today from such initial, almost perfect, smooth state.

Resolving this problem is once again dark matter, more precisely, cold dark matter (CDM). Unlike hot dark matter (HDM), which is relativistic and clusters poorly, cold dark matter is non-relativistic and can therefore cluster effectively [6]. Moreover, dark matter does not interact with photons—or at most only feebly, hence its name—and so does not couple to the baryonic-photon fluid. Rather, it forms its own pressureless fluid with zero sound speed, subject only to gravitational clustering. It is therefore free to cluster well before recombination. After recombination, baryonic matter can fall into the gravitational potential wells already established by dark matter. In this way, (cold) dark matter acts as indispensable catalyst for structure formation. Crucially, dark matter is not only essential for the structure formation, but the observed data are consistent with precisely the right ratio of baryonic to dark matter needed.

The CMB also provides more direct quantitative evidence. Performing the spherical Fourier transformation of the photon temperature field, and computing its variance yields the CMB power spectrum, which can be compared against predictions from inflationary Big-Bang cosmology [6]. This comparison is shown for Planck 2018 data in figure 2.2. In particular, the acoustic oscillations of the baryon-photon fluid manifest as peaks in the power spectrum, whose positions depend on the dark matter density and whose amplitude depends on the ratio of baryonic to dark matter. Global fits to this spectrum agree with high accuracy, making it the most precise method currently available for measuring dark matter density Ω_{DM}, surpassing the BBN models historically used.

2.2 Dark Matter Properties and Candidates

Whilst the gravitational evidence explored in the previous section is plentiful, much remains to be learnt about dark matter. Its mass, possible quantum numbers, decay width, production mechanism, and much more are still unknown [6]. To fully understand the nature of dark matter, its (possible) interactions with ordinary matter must be explored. Multiple different dark matter models and candidates have therefore been proposed. Before introducing some of these, a number of basic properties can be inferred directly from the gravitational evidence. Dark matter should be

- Matter: in the cosmological evolution, dark matter behaves as matter, with a density that scales inversely with volume $\rho_{\mathrm{m}} \propto a^{-3}$. This contrasts with radiation, which in addition to diluting with increasing volume also redshifts, giving $\rho_{\mathrm{r}} \propto a^{-4}$, and with dark energy, which to the best of our knowledge does not dilute at all.

- Cold: for the formation of large-scale structures in the Universe, dark matter must behave like a non-relativistic fluid from the time of matter-radiation equality onwards.

- Non-interacting (collisionless): although not completely non-interacting—some

interaction is generally required both for its production in the early Universe and for the possibility of detection today—any interaction beyond gravity with Standard Model particles must be negligible, otherwise it would likely already have been discovered. Dark matter is therefore commonly described as interacting only feebly, which is of course what motivates its name.

- Stable: dark matter must have been present since the early Universe through to today, placing a strong constraint on its decay rate (if a particle) or an analogous property for macroscopic objects (such as the evaporation rate for primordial black holes).

- Adiabatic: on cosmological scales, dark matter shares the same primordial density inhomogeneities as ordinary matter, implying a common mechanism for generating said inhomogeneity. This is attributed to quantum fluctuations of a single inflaton during cosmic inflation.

These properties constrain the nature of dark matter somewhat, though a vast range of possibilities remains. As an example, the valid mass range spans over 90 orders of magnitude [6]. Candidates are conventionally separated into three broad categories of increasing mass: field or wave dark matter, particle dark matter, and macroscopic objects. Although quantum field theory (QFT) fundamentally unifies fields and particles, it remains useful in practice to treat them separately, as the two descriptions are suited to different regimes. For lighter candidates with roughly $m \ll$ eV, the de Broglie wavelength is large enough that a classical field description is more appropriate, analogous to how a large number of photons are better described by classical electromagnetic fields. Conversely, for heavier candidates with roughly $m \gg$ keV, a particle description become more suitable. The remainder of this section briefly explores some of the many candidates in each category, as well as some alternative theories.

2.2.1 Dark Matter as Waves

At the heavier regime among the ultralight dark matter candidates best described as waves, $m \lesssim 1$ eV, are the so-called Weakly Interacting Slim Particles (WISP) [6]. These include, for instance, the axion and axion-like particles. Originally introduced in 1977 to dynamically explain the strong-CP problem, the axion is a hypothetical light pseudo-scalar. It arises as a Nambu–Goldstone boson from an additional $U(1)$ symmetry that is spontaneously broken [13]. Observational constraints require the axion to be feebly interacting, and it is stable over cosmological timescales, making it a viable dark matter candidate.

2.2.2 Dark Matter as Particles

None of the elementary particles in the Standard Model simultaneously satisfies all of the listed properties required of dark matter [6]. Historically, one early contender was the neutrino. Neutrinos are electrically neutral, weakly interacting, stable

particles with non-zero mass, and are highly abundant throughout the Universe. For several reasons, however, they prove inadequate as dark matter candidates. Most prominently, neutrinos were relativistic during matter-radiation equality, making them hot dark matter, which would have prevented them from forming the structure observed today. Whilst (quasi)-relativistic hot dark matter is ruled out, the cold requirement can actually be relaxed somewhat, leaving open the possibility of warm dark matter as an intermediate case.

If not a Standard Model particle, one might instead consider new hypothetical particles [6]. Such a particle could be completely uncharged under the Standard Model gauge groups, and may, for example, be a scalar singlet or an additional fermion. The latter encompasses what is known as a sterile neutrino—a heavier counterpart to the Standard Model neutrino, possibly associated with the right-handed neutrino absent from the Standard Model.

Alternatively, the new particle could carry charge under one or multiple of the Standard Model gauge groups [6]. Whilst observational constraints strongly restrict the possibility of electric charge, a small—almost negligible charge—is not completely ruled out, giving rise to so-called milli-charge dark matter. Another possibility is colour charge under $SU(3)$, though such models are heavily constrained since a coloured particle need to be confined within a hadron. Finally, the dark matter could carry charge under $SU(2)$ and therefore interact weakly. The common umbrella term Weakly Interacting Massive Particle (WIMP) has perhaps been the most prominent group of dark matter candidates. WIMPs would be thermally produced via the freeze-out mechanism (described in detail in section 2.3.1) and the predicted relic abundance (measure of leftover density that remained from the early Universe to now) naturally matches the observed dark matter density [13]. This coincidence is known as the WIMP miracle [6]. Historically, the WIMP has been a conceptually appealing candidate owing to the simplicity of the freeze-out mechanism and its potential connection to stabilising the electroweak scale against quantum corrections, offering a possible solution for the hierarchy problem (the concerning large difference in scale between the Higgs mass compared to the Planck mass).

A third possibility is that dark matter carries charge under an entirely new gauge symmetry. Indeed, additional forces beyond those of the Standard Model could have gone unnoticed if ordinary matter is neutral under them [14]. One can then imagine a scenario in which dark matter is neutral under the Standard Model groups but charged under this new gauge group, whilst ordinary matter is neutral under it [6]. Such hypothetical interactions are referred to as dark forces. In fact, there is no restriction to a single particle charged under said new groups. Much as the visible sector contains a rich spectrum of elementary particles, dark matter may be accompanied by a whole dark sector of particles. Within the possibility of dark forces, one might as usual imagine a variety of dark matter models, including for example scalar, fermionic, and vector dark matter charged under different dark groups. Even dark composite particles are a possibility, such as the dark glueballs: bound states of dark gauge bosons.

It is common to assume some form of portal interaction connecting the visible and dark sectors. A key limitation arises from gauge symmetry, which forbids renormalisable interactions between Standard Model fermions and new dark gauge fields or matter charged under them [14]. There is, however, one notable exception: the new dark group being Abelian and it coupling to the $U(1)$ group of the Standard Model. This give rise to a vector mediator, and is the model adopted in this thesis. Its underlying principles are explored in detail in section 2.5. Discarding interaction with the Standard Model fermions, additional portals are possible. The mediator could be spin-1/2 (neutrino), scalar (Higgs) or pseudo-scalar (axion) [15].

2.2.3 Dark Matter as Macroscopic Objects

Dark matter need not be a particle; it could instead be a macroscopic object that emits no light [6]. One class of such candidates is Massive Astrophysical Compact Halo Objects (MACHO), including planets, small dead stars or stray black holes. Since these consist of normal baryonic matter and are formed in the late Universe, they would require a large baryonic abundance and are therefore already ruled out by BBN and CMB constraints. A natural solution is that such objects formed before BBN, though this is not straightforward given the aforementioned problem of baryonic structure formation. One possibility is primordial black holes (PBH), formed from the primordial density inhomogeneities of the early Universe. These models are however subject to strong mass constraints, as the black hole must not have completely evaporated from Hawking radiation. Additional constraints arise from the fact that X-ray emissions from material accretion, an expected signature of black holes, have not yet been observed. Whilst PBH remain a viable dark matter candidate, interest in them has decreased, largely due to the discrepancy between the predicted number of such objects forming in the early Universe and the abundance required to account for dark matter [13].

2.2.4 Alternative Suggestions

The observations discussed so far provide compelling evidence for the existence of dark matter. Nevertheless, alternative theories have been proposed to explain these phenomena. One of the more popular alternatives is modified gravity, an idea that echoes the emergence of general relativity itself [6]. The astronomical observation of Mercury's orbit did not follow the predictions of Newtonian gravity, and this gravitational anomaly was initially thought to be resolved by an additional undiscovered planet, analogous to how the behaviour of Uranus had been explained by the discovery of Neptune. Ultimately, general relativity replaced Newtonian gravity and correctly accounted for the orbit. By analogy, the gravitational anomalies currently attributed to dark matter might instead be explained by a suitably modified theory of gravity.

One such attempt is Modified Newtonian dynamics (MOND) [13]. In essence, it began with postulating a modification to Newton's second law to $F = ma^2/a_0$ below some critical acceleration $a \ll a_0$, chosen such that the theory reproduced the observed

flat rotation curves. The original formulation was insufficient as a physical theory, as it conserved neither momentum, angular momentum, nor energy. However, it was actually never intended as a realistic theory, but rather as a weak-field limit of a more fundamental theory. What followed were incremental refinements. Aquadratic Lagrangian theory (AQUAL) resolves the conservation issues by modifying the Newtonian Lagrangian rather than the second law directly. Still, to replace general relativity, any such theory also need to account for phenomena such as gravitational lensing and cosmological expansion. Relativistic AQUAL (RAQUAL) was introduced to this end, describing the dynamics of matter and radiation with a modified metric supplemented by an additional scalar field contributing to the gravitation potential. Despite being more sophisticated, it still failed to correctly describe gravitational lensing, predicting it to be proportional to the baryonic matter alone. Observations, however, consistently show larger lensing, commonly attributed to the additional mass of dark matter. The leading MOND-based theory at present is Tensor-Vector-Scalar gravity (TeVeS). Containing two additional fields, three free parameters and one free function, the increased complexity comes at the cost of reduced predictive power.

Other approaches treat general relativity as a low-energy limit of a more fundamental theory [6]. One example is conformal gravity, imposing local conformal invariance of the action. Whilst it has been shown capable of reproducing flat rotational curves, it still faces several difficulties, including Ostrogradsky instability, ghost states at the quantum level, and an as-yet still unclear account of dark matter effects such as CMB and formation of large-scale structure.

More exotic explanations have also been proposed. One example is the suggestion that the observed dark matter density is a consequence of the infrared cut-off set by the horizon scale according to the holographic principle [16]. Although this more speculative attempt has shown success in reproducing the matter behaviour of dark matter and its current density ratio relative to baryonic matter, it has not been shown to cluster as cold dark matter yet.

2.3 Dark Matter Origins

Assuming dark matter to be a particle, its present abundance in the Universe may have arisen through several different mechanisms. The most prominent are thermal freeze-out and freeze-in, both involving interaction with visible matter.

2.3.1 Thermal Freeze-out

The thermal freeze-out scenario assumes dark matter, χ, to be a stable particle of mass m_χ that, in the early Universe, interacted with the thermal bath of Standard Model plasma at a rate exceeding the Hubble expansion rate H [6]. The early Universe was hot, and as long as $T > m_\chi$, dark matter annihilation $\chi\bar{\chi} \to l\bar{l}$ and creation $l\bar{l} \to \chi\bar{\chi}$ remained in equilibrium [17]. Dark matter was thus part of the thermal bath, sharing a common temperature with visible matter and maximising

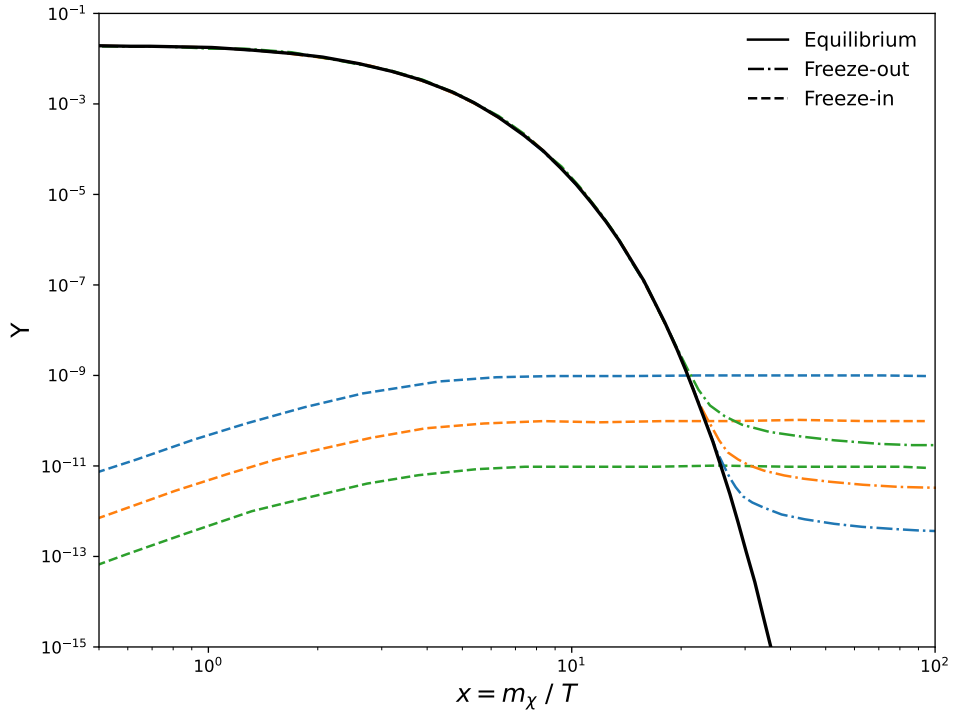

Figure 2.3: Illustration of the relic yield Y for freeze-out (dot-dashed line) and freeze-in (dashed line) as a function of $x = m_\chi/T$. The equilibrium yield is shown by the solid black line. The colours indicate the effect of a (generic, non-zero) coupling strength, increasing from green through orange to blue. Figure reproduced from figure 1 in [18].

entropy [6]. As the Universe expanded and cooled, production becomes suppressed once $T < m_\chi$, and the abundance of dark matter decreased exponentially [17]. This continued until the annihilation rate fell below the expansion rate H, at which point too few dark matter particles can interact and annihilate, resulting in the comoving density freezing at a fixed value. The present abundance of dark matter is this frozen relic of the annihilation process. This mechanism is illustrated in figure 2.3 as the dot-dashed line. Freeze-out is generally the most popular origin of dark matter.

2.3.2 Thermal Freeze-in

The thermal freeze-in scenario is effectively the inverse of freeze-out [18]. It assumes dark matter to interact so feebly with the visible matter plasma that it never was part of the thermal bath. Moreover, whether by inflation or some other mechanism, the abundance in the early Universe is assumed to be almost negligible. Importantly, despite the feeble interaction, they are not entirely absent such that a rare production of new dark matter gradually occurs. The dominant dark matter production takes place as $T < m_\chi$. As for thermal freeze-out, the abundance eventually stabilises, remaining fixed to the present day. The key distinction is directional: freeze-out moves away from thermal equilibrium as it stabilises, whilst freeze-in approaches towards thermal equilibrium as it stabilises. Freeze-in is illustrated by the dashed

lines in figure 2.3. Notably, freeze-in is particularly interesting because of its model simplicity, explaining the dark matter relic with a minimal set of particle properties.

2.4 Dark Matter Searches

In order to learn more about dark matter beyond what gravitational observations alone can tell us, its possible interaction with ordinary matter must be studied. So far, no such interaction has been observed. Nonetheless, there exist three main search strategies: direct detection, indirect detection, and detection at accelerators, each of which is briefly introduced below [6].

Earth resides within the dark matter halo, constantly moving through a flux of dark matter particles that could interact with visible matter [6]. Direct detection attempts to observe the recoil of atomic nuclei or electrons produced by such interactions. The main challenge is that dark matter scattering rates are extremely small, as is the energy deposited. Consequently, direct detection experiments are typically located deep underground and constructed of ultra-pure materials to minimise background.

Indirect detection instead searches for the products of dark matter annihilation or decay in our Galaxy and other astrophysical environments, by studying cosmic ray fluxes arriving at Earth [6]. Rather than detecting dark matter itself, it looks for ordinary Standard Model particles that may have been produced from such dark matter processes.

Finally, detection at accelerators takes a different approach altogether. Instead of directly or indirectly searching for dark matter already present in our Galaxy, it aims to produce dark matter in a controlled environment at particle accelerators [6]. Once produced, the dark matter must still be detected which is done either analogously with direct experiments—by measuring nuclei or electron recoils—or through missing energy or momentum signatures. The latter exploits the fact that feebly interacting dark matter may escape the detector entirely, carrying away energy and momentum.

This thesis focuses on detection at accelerators, specifically at proton beam fixed-target experiments, where a high-energy beam is directed at a stationary target. These detect dark matter through direct recoil measurements. Henceforth, the term "direct detection" refers exclusively to direct detection at accelerators, not to be confused with direct detection of passing dark matter in our Galaxy, unless explicitly stated otherwise.

2.5 Light Dark Matter and the Vector Portal Model

From the previous sections, it is clear that the possible range of dark matter candidates and masses is enormous. The thermal freeze-out hypothesis restricts this mass range

somewhat. An upper bound is set by quantum-mechanical unitarity constraints on the annihilation amplitude, whilst a lower bound is set by the requirement that dark matter does not cluster and form structure too early [19]. The resulting allowed region is thus restricted down to roughly $\sim$ [keV, 100 TeV]. Historically, one of the most prominent candidates were WIMPs, with masses above the GeV scale. These regions have consequently been searched thoroughly, yet without yielding any result. Recently, for precisely this reason, attention has shifted away from WIMPs towards light dark matter (LDM) candidates in the sub-GeV region.

To fit within the freeze-out framework, LDM must interact feebly with visible matter in order to initially be part of the thermal bath. Naively, one might then suppose that this interaction proceeds extremely feebly through the electroweak force. There is reason to doubt this, however. In particular, the current observed abundance of dark matter requires a sufficient depleting of the large dark matter entropy, a condition that feebly interacting electroweak dark matter would not satisfy [20]. A more promising alternative is that dark matter carries charge under an additional dark force, with some portal interaction connecting the dark and visible sector. As previously discussed, this can be realised by introducing an additional Abelian group, denoted $U(1)'$, accompanied by a new (dark) vector mediator.

2.5.1 The Lagrangian

This thesis adopts the benchmark model of a light complex scalar dark matter particle χ, accompanied by a new vector mediator called the dark photon A'_μ, serving as the gauge boson of $U(1)'$. Additional dark sector particles may be present, but are not relevant to this analysis and are therefore neglected. The Lagrangian is [7]

$$\mathscr{L} \sim \mathscr{L}_{\mathrm{SM}} + \mathscr{L}_\chi + \mathscr{L}_{A'}. \tag{2.3}$$

Here, $\mathscr{L}_{\mathrm{SM}}$ is the Standard Model Lagrangian. The two new terms describe the dark matter and the dark photon respectively. The dark matter term contains, as usual, a kinetic term, a mass term, and an interaction term, the last of which couples dark matter to the dark photon in direct analogy with electromagnetism

$$\mathscr{L}_\chi = \mathscr{L}_\chi^{\mathrm{free}} - \mathscr{L}_\chi^{\mathrm{pot}} + A'_\mu J^\mu_\chi. \tag{2.4}$$

The explicit form of these terms depends on the dark matter model—whether, for example, it is a complex scalar or a Dirac spinor. Regardless, the dark matter is charged only under the dark $U(1)'$ gauge group, so the covariant derivative takes the form $D_\mu = \partial_\mu - i g_D A'_\mu$, where g_D is the $U(1)'$ gauge coupling strength. Due to the large constraints excluding most regions of Dirac spinor dark matter, this thesis focuses on the case of a complex scalar, described by the complex Klein–Gordon equation

$$\mathscr{L}_\chi = D_\mu \chi^\dagger D^\mu \chi - m^2 \chi^\dagger \chi = \partial_\mu \chi^\dagger \partial^\mu \chi - m^2 \chi^\dagger \chi + A'_\mu J^\mu_\chi + \mathcal{O}(g_D^2), \tag{2.5}$$

where $A'_\mu J^\mu_\chi \equiv i g_D A'_\mu [\chi^\dagger(\partial_\mu \chi) - (\partial_\mu \chi^\dagger)\chi]$, consistent with the general expression in equation (2.4). The final term, $\mathcal{O}(g_D^2)$, describing a four-point interaction, is subdominant compared to the three-point processes and thus conventionally neglected.

A massless dark photon would not couple directly to any Standard Model current, coupling instead only to operators with dimension four or higher, such as the magnetic moment or the charge form factors [15]. If instead the dark photon would acquire mass, then it would couple to the electromagnetic current. Mass can be acquired through, for example, the Stückelberg mechanism or the Higgs mechanism via spontaneous breaking of the dark Higgs vacuum expectation value. Here, a massive vector mediator is assumed. The corresponding Lagrangian term is then

$$\mathscr{L}_{A'} = -\frac{1}{4}F'_{\mu\nu}F'^{\mu\nu} + \frac{1}{2}m^2_{A'}A'_\mu A'^\mu + \frac{1}{2}\epsilon F'_{\mu\nu}F^{\mu\nu}. \tag{2.6}$$

The first term is the kinetic term, in analogy with electromagnetism, the second is the mass term, and the third term is the vector portal term, through which the dark photon couples to the Standard Model photon. The strength of this kinetic mixing is set by ϵ, called the kinetic mixing parameter. It generally acts like a free parameter satisfying $\epsilon \ll 1$ [20].

There are essentially two choices regarding the kinetic mixing. Either the $U(1)'$ mixes kinetically with the hypercharge group $U(1)_Y$ (written in the gauge basis before spontaneous symmetry breaking), with $F_{\mu\nu} = \partial_{[\mu}B_{\nu]}$ in the equation above, or with the electromagnetic-charge group $U(1)_{\text{em}}$ (written in mass basis after spontaneous symmetry breaking), with $F_{\mu\nu} = \partial_{[\mu}A_{\nu]}$ [15]. Here, B_μ denotes the hypercharge field and A_μ the Maxwell field. The appropriate choice depends on the relevant energy scale. Below the electroweak scale, where the electroweak symmetry is broken, the coupling should be applied to the Maxwell field A_μ. In contrast, above the electroweak scale the symmetry remains unbroken and the coupling should be to the hypercharge field B_μ, which additionally leads to a small mixing between the Z-boson and the dark sector. Although proton beam experiments are high-energy, the relevant interactions occur at energy scales below electroweak scale. Therefore, this thesis adopts the commonly used second alternative: kinetic mixing via $U(1)_{\text{em}}$.

To diagonalise the kinetic terms in equation (2.6), the following field redefinition is performed

$$\begin{aligned} A_\mu &\to A_\mu + \epsilon A'_\mu, \\ A'_\mu &\to \frac{1}{\sqrt{1-\epsilon^2}}A'_\mu. \end{aligned} \tag{2.7}$$

Applying this transformation to diagonalise also affects the gauge-current couplings in both the dark matter and Standard Model Lagrangian

$$\begin{aligned} \mathscr{L}_\chi \supset A'_\mu J^\mu_\chi &\to \frac{1}{\sqrt{1-\epsilon^2}}A'_\mu J^\mu_\chi \simeq A'_\mu J^\mu_\chi \\ i\bar{\psi}\not{D}\psi \supset eA_\mu J^\mu_{\text{em}} &\to eA_\mu J^\mu_{\text{em}} + e\frac{\epsilon}{\sqrt{1-\epsilon^2}}A'_\mu J^\mu_{\text{em}} \simeq eA_\mu J^\mu_{\text{em}} + e\epsilon A'_\mu J^\mu_{\text{em}} \end{aligned} \tag{2.8}$$

The total Lagrangian is therefore approximately

$$\mathscr{L} = \mathscr{L}_{\text{SM}} + \partial_\mu\chi^\dagger\partial^\mu\chi - m^2\chi^\dagger\chi - \frac{1}{4}F'_{\mu\nu}F'^{\mu\nu} + \frac{1}{2}m^2_{A'}A'_\mu A'^\mu + e\epsilon A'_\mu J^\mu_{\text{em}} + A'_\mu J^\mu_\chi, \tag{2.9}$$

and serves as the underlying Lagrangian in this thesis.

2.5.2 Model Parameters

As apparent from the Lagrangian, equation (2.9), the model is fully characterised by four parameters $\{\epsilon, g_D, m_\chi, m_{A'}\}$. It is conventional to define a dark fine-structure constant $\alpha_D \equiv g_D^2/(4\pi)$ in analogy to the ordinary fine-structure constant $\alpha = e^2/(4\pi)$, replacing g_D as one of the four model parameters. These four parameters are common regardless of whether the dark matter is a complex scalar, Dirac spinor, or Majorana spinor [20]. Moreover, in most such models the annihilation cross section relevant for freeze-out has the same parametric scaling in the limit $m_{A'} \gg m_\chi$

$$\sigma v_{\text{rel}}(\chi\chi^\dagger \to A' \to f\bar{f}) \propto \frac{\epsilon^2 \alpha_D m_\chi^2}{m_{A'}^4}, \tag{2.10}$$

where v_{rel} is the relative velocity between the annihilated dark matter particles. It is therefore convenient to introduce a dimensionless interaction strength parameter

$$y \equiv \epsilon^2 \alpha_D \left(\frac{m_\chi}{m_{A'}}\right)^4, \tag{2.11}$$

such that $\sigma v_{\text{rel}}(\chi\chi^\dagger \to A' \to f\bar{f}) \propto y/m_\chi^2$. When displaying constraints on the model parameters, it is customary to fix benchmark values for α_D and the ratio $m_{A'}/m_\chi$. Sensitivity plots then typically display the plane spanned by y and either m_χ or $m_{A'}$, with contours of constant signal events. These plots are discussed in greater detail in section 3.6. This thesis adopts the benchmark values $\alpha_D = 0.1$ and $m_{A'}/m_\chi = 2.5$.

2.6 Concerning Mesons

Due to its central role in this thesis, a brief review of mesons is in order. The Standard Model contains four fundamental types of particles; quarks, leptons, gauge bosons, and the Higgs boson [21]. In particular, quarks are fermionic particles transforming as the fundamental representation under $SU(3)$: they are coloured. The phenomenon of colour confinement dictates that coloured particles cannot exist in isolation. Quarks are therefore strongly bound together into colour-neutral composite particles called hadrons, further separated into two categories: baryons, consisting of three differently coloured quarks (the proton and neutron being familiar examples), and mesons, which contain a quark and its antiquark, or a superposition of such states.

Since each quark is a spin-1/2 fermion, a meson is bosonic. The two fermions can combine with spins either aligned parallel or antiparallel, yielding a spin singlet ($S = 0$) or spin triplet ($S = 1$). Combined with the orbital angular momentum $\vec{L}$, the total angular momentum $\vec{J}$ satisfies $|L - S| \leq J \leq L + S$. Particles are commonly labelled J^{PC}, where $P = \pm$ is even or odd parity $(-1)^{L+1}$ and $C = \pm$ is even or odd charge conjugation $(-1)^{L+S}$. Mesons with 0^{++} are called scalar mesons, 1^{--} are vector mesons, and 0^{-+} are called pseudo-scalar mesons. Analogously, there exist, for example, also pseudo-vector mesons, axial-vector mesons and tensor mesons. The pseudo-scalar mesons π^0 and η (and the vector meson ω) have important primary dark matter production channels. The vector mesons ρ, ω and ϕ are instead of central importance for the new secondary production channel.

3

Proton Fixed-Target Experiments

Following the null results of searches for WIMP dark matter, attention has indeed shifted towards the possibility of LDM. As previously discussed, the vector portal model has emerged as a plausible candidate for such LDM compatible with thermal freeze-out. However, these LDM candidates carry too little kinetic energy to be accessible to traditional direct detection experiments, relying on galactic dark matter passing through the Earth as it moves within the dark matter halo [22]. Accelerator-based detection has consequently gained traction as a more viable approach. In particular, fixed-target experiments—where a high-energy beam, whether electron or proton, collides with a stationary target—have become a focus of considerable interest. This chapter presents the topic of proton beam experiments. It begins with a brief comparison with electron beam experiments, before describing some of the more prominent proton beam experiments. Subsequently, the primary production channels and detection strategies are discussed. The chapter closes with an introduction to the two simulation tools used in this thesis to study the sensitivity at proton beam experiments, as well as the statistics used to obtain the results.

3.1 Proton Beam vs Electron Beam

As discussed in section 2.4, accelerator-based experiments may detect produced dark matter through different methods. The two most prominent are missing energy or momentum and direct detection via downstream scattering. The former is realised primarily at electron beam experiments, where individual electrons are tagged before hitting the target [8]. If dark matter is produced in the collision, it may escape the detector without interacting, carrying away energy and momentum. By measuring the energy loss of the electrons alongside the absence of other possibly produced particles that could account for the missing energy or momentum, dark matter events may be identified. NA64 is an example of an electron beam experiment exploiting missing energy, whilst the proposed LDMX will use the missing momentum approach. One immediate limitation of the electron beam experiments is the requirement to tag individual incoming electrons, which places an upper limit on the beam intensity.

Protons, being hadrons, interact less cleanly, making individual tagging impractical and therefore missing energy or momentum detection far less viable. Instead, they

predominantly rely on direct detection methods, measuring dark matter scattering off electrons or nuclei in the downstream detector [7]. This, however, significantly reduces the signal yield. At an electron beam, the yield scales as ϵ^2 from the dark matter production through kinetic mixing. At a proton beam, production introduces the same factor ϵ^2, but detection requires dark matter to scatter with a Standard Model particle once more through kinetic mixing, introducing an additional factor of $\alpha_D\epsilon^2$, giving a total of $\alpha_D\epsilon^4$. Nevertheless, the proton beam experiments compensate by allowing a higher beam power (made possible by the absence of tagging), as well as through additional production channels not available at electron beams.

3.2 Experimental Configurations

Various proton beam experiments exist that either are dedicated, or at least capable of detecting LDM. Some of these are established experiments and currently operational, whilst others are still in development. This section introduces the experiments studied in this thesis, with particular focus on their experimental layouts, which must be implemented in the simulations.

3.2.1 SHiP

SHiP, an abbreviation of Search for Hidden Particles, is a proposed general-purpose experiment at the CERN Super Proton Synchrotron (SPS) [7]. It will focus on long-lived weakly interacting particles with mass $m < 10$ Gev, including neutrinos (notably, it is expected to provide the first ever direct detection of the tau antineutrino, thereby completing the list of directly detected Standard Model particles), as well as various Beyond the Standard Model (BSM) particles, such as LDM. Initial installation of the detector is currently planned for 2029–2032, with data collection beginning in 2033 [23].

The general experimental layout consists of a 400 GeV proton beam directed onto a thick heavy-metal hybrid target [7]. Downstream of the target, a hadron stopper absorbs any escaping Standard Model particle produced in the beam interaction, followed by a muon shield. The signal thereafter should thus be clean, containing only hidden sector particles and neutrinos. The primary background for detecting LDM is therefore neutrinos. Next is the Scattering and Neutrino Detector (SND), specifically designed for LDM searches and is therefore the component of primary interest for this thesis. The experiment concludes with a long vacuum decay vessel and a Hidden Sector Detector aimed at searching for any long-lived BSM particles.

SHiP was previously proposed to be built in the ECN4 cavern, with a target consisting of titanium-zirconium doped molybdenum alloy followed by blocks of tungsten, and a lead detector of dimensions $0.9 \times 0.75 \times 3.21$ m^3 (W×H×D) [7]. The detector would be positioned at $(x, y, z) = (0, 0, 38)$ m relative to the centre of the beam dump target, with z pointing along the beam direction. Over a proposed 5 year operation, the experiment would accumulate a total of 2×10^{20} protons on target (POT). Following previous studies, such as [24], the target is well approximated as a

Table 3.1: Experimental design for SHiP, DUNE ND and NOνA ND as used in the simulations performed with MadDump and Pythia. Both the old ECN4 design and the new ECN3 are shown for SHiP, and both the target and targetless versions of DUNE are shown. Total flux is computed over the full operational period. Distance refers to the distance from the target to the detector along the beam axis. Parameters for ECN4 have been assembled from [7] and ECN3 from [23]. For DUNE ND, the parameters are collected from [26], [27], [28], [29], whilst parameters for NOνA ND are taken from [26], [30], [31], [32], [33].

	SHiP		DUNE ND		NOνA ND
	ECN4	ECN3	Target	Targetless	
General					
Operation [yr]	5	15	7	7	-
Beam energy [GeV]	400	400	120	120	120
Total flux [POT]	2e20	6e20	7.7e21	7.7e21	2.97e20
Target					
Material	^{96}Mo	^{184}W	^{12}C	^{27}Al	^{12}C
Detector					
Material	^{207}Pb	^{184}W	^{40}LAr	^{12}C	CH_2
Z average	82	74	18	18	2.67
A average	207	184	40	40	4.67
Distance [m]	38	25	574	304	990
Density [g/cm^3]	5.0	7.08	1.3954	1.3954	0.9
x [cm]	90.3	40	700	700	380
y [cm]	74.9	40	300	300	380
z [cm]	321	150	500	500	1280
radius [m]	-	-	2.59	-	2.14
yc [m]	-	-	0, 6, 12, 18, 24	-	14.46

uniform molybdenum block.

An alternative configuration has been proposed and approved for the ECN3 facility [25]. Modifications include changing the target material to tungsten, the detector to one composed alternating tungsten and silicon plates, and an extended operation period to 15 years, yielding a total of 6×10^{20} POT [23]. Further parameters relevant to this thesis for both the ECN4 and ECN3 configurations are listed in table 3.1, alongside those for the other two proton beam experiments considered. Although SHiP might still be subject to further design changes, this is the most recent approved design.

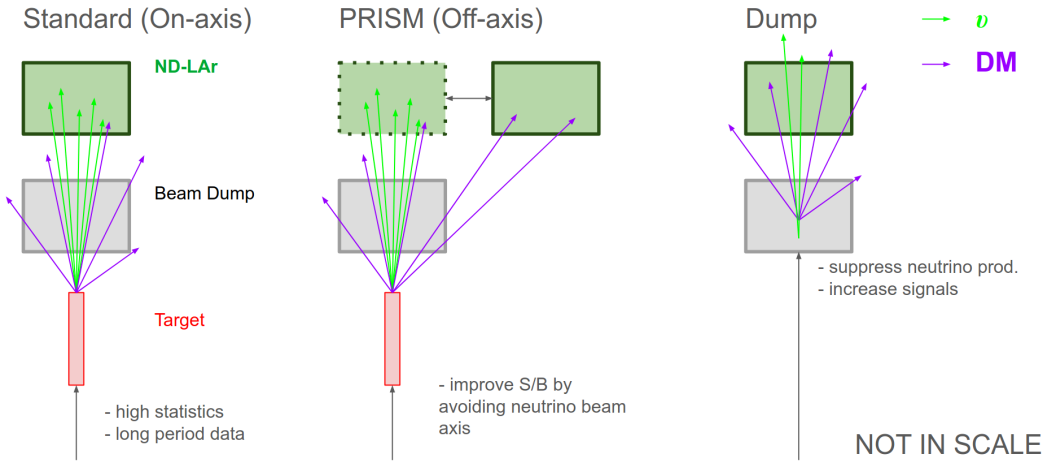

Figure 3.1: Illustration of the different operating modes for LDM searches at DUNE ND. From left to right: on-axis (target), off-axis (PRISM), and beam dump (targetless). Figure from [35].

3.2.2 DUNE ND

Conceived in 2015, the Deep Underground Neutrino Experiment (DUNE) is a 120 GeV proton beam experiment expected to begin operation in 2029 [34]. The proton beam is directed at a low-Z fixed carbon target, where various particles such as mesons, baryons and other unstable intermediate particles are produced [26]. These unstable particles are transported through a decay pipe, where they decay into stable particles, including photons and neutrinos. DUNE comprises two detectors: a near detector (ND) situated 574 m downstream of the target, and a far detector (FD) approximately 1300 km away [27]. A thick high-Z hadron absorber is placed 221 m from the target, designed to stop any hadrons not yet decayed [28].

As its name suggests, DUNE is primarily a neutrino experiment, and can operate in both a neutrino and anti-neutrino mode. Nevertheless, the ND can also serve as a detector for LDM [27]. It is a $7 \times 3 \times 5$ m^3 (W×H×D) liquid argon (LAr) detector with a fiducial mass of 50 tonnes. As with SHiP, the main source of background is neutrinos. However, being a dedicated neutrino experiment with a different experimental layout, DUNE is subject to considerably more neutrino background than a purpose-built LDM detector [29]. Two feasible approaches to reducing this background have been proposed: off-axis detection and targetless detection, both illustrated alongside the baseline setup in figure 3.1.

The first approach exploits the PRISM (Precision Reaction-Independent Spectrum Measurement) mechanism, which allows the ND to move off-axis [27]. The produced neutrinos originate from charged meson decays, and are focused by a magnetic horn system [36]. They therefore travel narrowly forward. LDM, by contrast, would originate predominantly from neutral meson decay and thus be more isotropically distributed. Moving the detector off-axis therefore improves the signal-to-background ratio, albeit at the cost of significant reduction in total signal yield.

Alternatively, the low-Z target can be removed and the proton beam directed straight into the hadron absorber [29]. This targetless configuration would essentially transform DUNE ND to a proton beam dump experiment like SHiP, substantially reducing the neutrino background since the charged mesons are absorbed in the hadron absorber (beam dump). It also increases the photon flux and reduces the effective distance to the detector. Whilst this configuration is not reasonable for long term detection—as it would interfere with the main purpose of neutrino analysis—it is assumed to be feasible for the purposes of this thesis.

Originally designed with a (upgradable) 1.2 MW wide-band neutrino beam corresponding to 1.1×10^{21} POT/year, DUNE has received a phase II strategy [34]. Plans include, among other things, to continuously upgrade the experiment over 15 years of operation, ultimately reaching a 2.4 MW beam, adding two additional FD modules, and improving the ND. None of these upgrades are taken into account in the analysis presented here. Instead, following [26] and [27], a 7 year run of 1.1×10^{21} POT/year is assumed. Furthermore, following [29], the beam dump is assumed to consist of a thick aluminium block. All relevant specifications are listed in table 3.1.

3.2.3 NOνA ND

NOνA (NuMI Off-Axis ν_e Appearance Experiment) is a currently operating off-axis neutrino experiment optimised to study the oscillation of muon neutrinos into electron neutrinos [37]. Like DUNE, it comprises a far detector (FD) located 810 km away from the target, and a near detector (ND). Relevant for the LDM searches is the ND, situated 990 m downstream of the graphite target, struck by a 120 GeV proton beam [26]. The detector is positioned 14.6 mrad off-axis, consists of a liquid scintillator based primarily on mineral oil [33], and has dimensions $3.8 \times 3.8 \times 12.8$ m^3 (W×H×D) [31]. For simulation purposes, the detector material is approximated as CH_2, with a density taken to be 0.9 g/cm^3. Since NOνA is an operating experiment, the total POT depends on the dataset and run period used. Following [26], [30], [32] a total of 2.97×10^{20} POT is used. The main specifications used are presented in table 3.1.

3.3 Primary Production Channels

At energies below the electroweak scale, the mixing between the Standard Model and the dark photon proceeds through $e\epsilon A'_\mu J^\mu_{\text{em}}$, as seen in equation (2.9). Apart from the kinetic mixing parameter ϵ, this interaction is identical to the coupling between the photon and charged fermions. Consequently, the dark photon can be produced through the same mechanism as the ordinary photon. The main ones are [15]

- Bremsstrahlung: $e^- Z \to e^- Z A'$
- Proton bremsstrahlung: $pZ \to pZA'$
- Annihilation: $e^- e^+ \to \gamma A'$

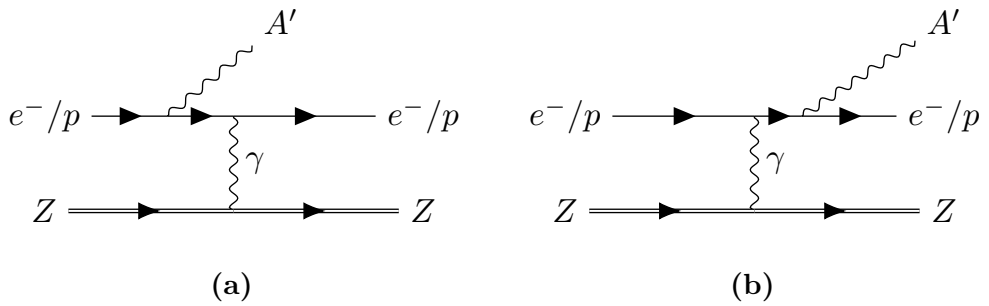

Figure 3.2: Feynman diagrams of bremsstrahlung (electron or proton) production of dark photon, showing (a) initial-state radiation, and (b) final-state radiation.

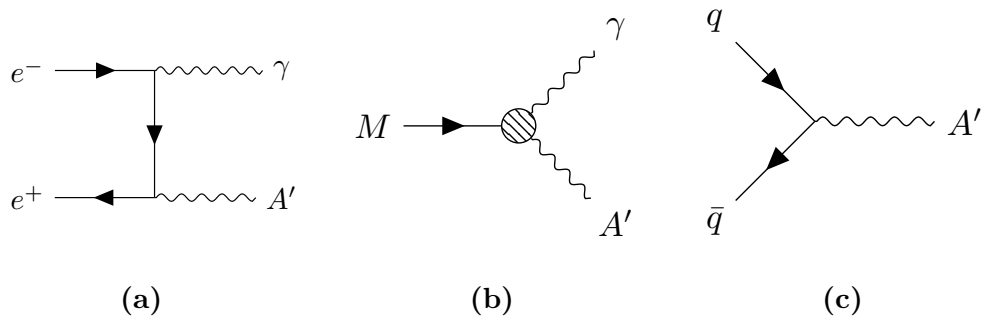

Figure 3.3: Feynman diagrams of dark photon production via (a) annihilation, (b) meson decay, and (c) Drell–Yan processes.

- (Light) meson decay: $M \to \gamma A'$
- Drell–Yan: $q\bar{q} \to A'$

These production mechanisms are illustrated in figure 3.2–3.3. For proton beam experiments, the relevant channels are proton bremsstrahlung, meson decay and Drell–Yan [7]. However, Drell–Yan production is only relevant at higher masses $m_{A'} \gtrsim 1$ GeV and can therefore be safely neglected for sub-GeV dark matter [7].

Once produced, a dark photon can either decay visibly into Standard Model particles, such as a quark-antiquark pair or a lepton-antilepton pair, or invisibly into dark matter [15], see figure 3.4. Energy conservation requires $m_{A'} > 2m_\chi$ for on-shell dark matter production. Moreover, if $\alpha_D \gg \alpha\epsilon^2$, the invisible channel dominates and

$$\mathrm{BR}(A' \to \chi\chi^\dagger) \simeq 1. \tag{3.1}$$

Since the parameter region relevant to the proton beam experiment satisfies both these conditions, this branching ratio is adopted throughout.

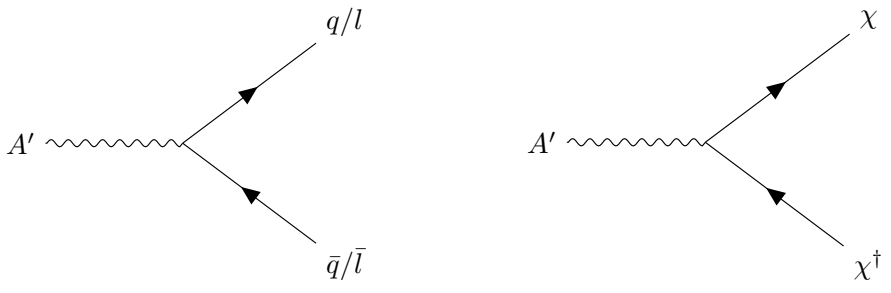

(a) **(b)**

Figure 3.4: Feynman diagrams of dark photon decay into (a) visible Standard Model particles (quark-antiquark or lepton-antilepton pairs) or (b) dark matter.

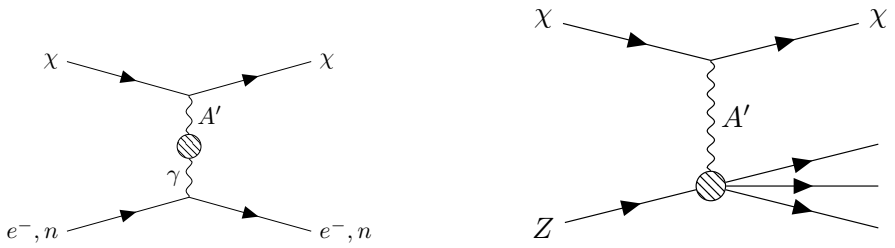

(a) **(b)**

Figure 3.5: Feynman diagrams of dark matter scattering: (a) elastic scattering off electrons or nucleons, (b) deep-inelastic scattering (DIS) off nuclei.

3.4 Detection Strategies and Background

At proton beam experiments, dark matter is searched for through direct detection. Once produced, a dark matter particle travels towards the detector, where it may scatter off the detector material via kinetic mixing and subsequently be detected. The main detection channels are

- Elastic scattering off electrons
- Elastic scattering off (nucleons in) nuclei
- Deep inelastic scattering (DIS) off (quarks in) nuclei

Each of these is illustrated in figure 3.5. Elastic electron scattering is the dominant detection channel, largely due to its considerably lower background compared to the other two [7]. To improve signal-to-background ratios, appropriate kinematic cuts are imposed. For electron scattering at SHiP, the optimal selection window established in [7], is

$$E_e \in [1, 5] \text{ GeV}, \qquad \theta_e \in [10, 30] \text{ mrad}, \tag{3.2}$$

where E_e is the recoil electron energy and θ_e is the polar angle with respect to the incoming dark matter particle

$$\theta_e \equiv \arccos\left(\frac{\vec{p}_\chi \cdot \vec{p}_e}{|\vec{p}_\chi||\vec{p}_e|}\right). \tag{3.3}$$

For DUNE, the selection window adopted from [26] is instead

$$E_e\theta_e^2 < 2 \text{ MeV rad}^2, \tag{3.4}$$

and for NOνA, consistent with [30], the following kinematic cuts are used

$$E_e\theta_e^2 < 5 \text{ MeV rad}^2, \qquad E_e \in [0.5, 5] \text{ GeV}. \tag{3.5}$$

The dominant background in all experiments consists of neutrinos, which produce signatures closely resembling those of LDM. For the original ECN4 design of SHiP, the background from [7] is used, assuming 5 years of operation and the kinematic cuts of equation (3.2). For the ECN3 design, the background is scaled linearly with the three times longer operation period. The neutrino background for the on-axis and off-axis DUNE ND configurations, applying the kinematic cuts of equation (3.4), is taken from the thorough discussion in [26]. For the targetless beam dump configuration, neutrino flux is approximately reduced by a factor of 10^{-3} relative to the standard target configuration [29]. Lastly, the background for NOνA from [30] is adopted, with the kinematic cuts of equation (3.5). All values are collected in table 3.2. Note that whilst SHiP and NOνA quote total background events for the full run, DUNE values are given per year per tonne. The ECN3 and targetless DUNE configurations are omitted from the table, as their backgrounds follow directly from the scalings previously described.

For the secondary photoproduced vector meson decay channel studied in the next chapter, deep inelastic scattering and elastic scattering nucleon scattering are also considered, the analysis is however restricted to SHiP ECN4. For deep inelastic scattering, 9000 background events are assumed, consistent with [38]. The same value is also adopted for elastic scattering off nucleons. No kinematic cuts are applied for these.

3.5 Simulation Tools

To study the sensitivity of the primary dark matter production channels across different proton beam experiments, the primary tool is MadDump[1], a plugin to the simulation framework MadGraph5_aMC@NLO[2]. For simulating meson decays, MadDump requires meson spectra from an event generator such as Pythia[3], which is used in this thesis. This section presents both tools and the methodology for using them. Whilst MadDump will prove insufficient to study the secondary invisible meson decay channel—the focus of the next chapter—Pythia will also play an important role there.

[1]Trunk series revision 57, available at https://launchpad.net/maddump.
[2]Version 2.6.7, available at https://launchpad.net/mg5amcnlo.
[3]Version 8.317, available at https://www.pythia.org.

Table 3.2: Expected neutrino backgrounds for the experiments after applying the respective kinematic cuts described in the text. For DUNE, the background is given per year per tonne, for neutrino (antineutrino) mode, and for the on-axis configuration and each considered off-axis position. For NOνA, only the total event count is provided.

	SHiP	DUNE ND					NOνA ND
	ECN4	On-axis	6 m	12 m	18 m	24 m	-
ν_e	77	9 (3)	6 (2)	4 (2)	2 (1)	1 (0)	-
$\bar{\nu}_e$	55	1 (3)	1 (2)	1 (1)	0 (1)	0 (0)	-
ν_μ	60	115 (12)	78 (10)	27 (5)	13 (3)	7 (2)	-
$\bar{\nu}_\mu$	38	8 (82)	6 (45)	3 (20)	2 (9)	1 (5)	-
ν_e-CCQE	-	14 (3)	10 (3)	6 (2)	3 (1)	2 (1)	-
Total	230	147 (103)	101 (62)	41 (30)	20 (15)	11 (8)	580

3.5.1 MadDump

MadDump is a plugin to the general-purpose software framework MadGraph5_aMC@NLO, hereafter referred to simply as MadGraph5. In essence, MadGraph5 is a framework for automated computation of cross sections up to next-to-leading order, simulation of parton showers, and merging of samples [39]. It supports both Standard Model physics and BSM physics through user-specified Lagrangians, implemented via the Mathematica package FeynRules and supplied to MadGraph5 through a UFO (Universal FeynRules output) file. For the purposes of this thesis, it suffices to regard MadDump as a plugin that simplifies the full chain of subprocesses for BSM detection at beam experiments, automating the complete chain from production to detection [38]. The discussion here is restricted to the details needed to run the simulations; for a thorough description of how the plugin works, see the original publication [38].

Once installed, the most convenient way of specifying experimental details is through an input card. Example layouts are provided in appendix A. Each card begins by specifying the UFO file, encoding information about the Lagrangian. Throughout this thesis, the model `DM_mesons_2` included in the `example_SHiP` directory distributed with MadDump is used. It contains, among other things, the structure for complex scalar dark matter, denoted `Xc`, and the dark photon, denoted `Y1`.

The procedure for specifying specific production channel varies slightly between channels. Certain processes can be provided and simulated directly within MadDump. One such example is Drell–Yan processes. Another is proton bremsstrahlung, which although not part of the mature release, is implemented in the development version using the Fermi–Williams–Weizsäcker method, as outlined in [7]. This approach effectively includes off-shell mixing with vector mesons such as ρ and ω, and therefore exhibits a resonance structure around their masses. Other processes, such as hadronic decays, require external event generators to produce the intermediate particles. A relevant example is the meson decay channels, which require an external model of the

produced meson spectrum to be subsequently decayed within MadDump. This can be modelled using the event generator Pythia, and then provided in the conventional HepMC format. Thereafter, the decay itself is specified in the input card.

The basic geometry of the detector can be specified for both on-axis and off-axis configurations [38]. For the former, two native detector shapes are supported: parallelepiped and cylinder. All on-axis experiments considered in this thesis use the parallelepiped geometry, enabled by the following commands

```
set parallelepiped True
set x_side value
set y_side value
set depth value
```

For the off-axis case, only a truncated cone shape is natively supported. Whilst it is possible to hard-code a custom detector shape, the truncated cone approximation is used here for all off-axis configurations, enabled by

```
set off_axis True
set yc value
set radius value
set depth value
```

where `yc` is the distance from the beam axis and `depth` is the detector length projected along the beam axis. The approximate radii used for the off-axis detector configurations are provided in table 3.1. When inputting values, MadDump assumes all lengths are provided in cm and masses in g. Common to all detector geometries are the following commands

```
set d_target_detector value
set detector_density value
set Z_average value
set A_average value
```

It is worth noting that MadDump supports only detection via elastic electron scattering and DIS, not elastic nucleon scattering [38]. Since elastic electron scattering is dominant across the majority of the mass range considered, it is standard practice to include only this detection channel.

The main output of MadDump includes event files containing kinematic information for the processes, and a `scan_run` file of the predicted number of detected dark matter events for each detection mode at each simulated mass. The kinematic information can then be used to apply the kinematic cuts of equation (3.2), (3.4) or (3.5).

MadDump assumes a unit branching ratio for the meson decay to dark photon, so an appropriate scaling factor must be applied. One convenient choice is to compute the ratio of the invisible decay to that of the corresponding visible Standard Model decay [7]

$$\begin{aligned} \frac{\mathrm{BR}(\pi^0, \eta \to \gamma A')}{\mathrm{BR}(\pi^0, \eta \to 2\gamma)} &\simeq 2\epsilon^2 \left(1 - \frac{m_{A'}^2}{m_{\pi^0,\eta}^2}\right)^3 \\ \frac{\mathrm{BR}(\omega \to \pi^0 A')}{\mathrm{BR}(\omega \to \pi^0 \gamma)} &\simeq \epsilon^2 \left(\frac{[m_{A'}^2 - (m_\pi + m_\omega)^2][m_{A'}^2 - (m_\pi - m_\omega)^2]}{(m_\omega^2 - m_\pi^2)^2}\right)^{3/2} \end{aligned} \tag{3.6}$$

Since the Standard Model branching ratios are known from experiment, the scaling factors are determined for any given dark matter and dark photon mass. In particular, $\mathrm{BR}(\pi^0 \to 2\gamma) \simeq 98.8\%$, $\mathrm{BR}(\eta \to 2\gamma) \simeq 39.4\%$ and $\mathrm{BR}(\omega \to \pi^0\gamma) \simeq 8.3\%$ [40].

Similarly, the proton bremsstrahlung output does not include the full coupling scaling and must be multiplied by a factor of $\alpha\epsilon^2$.

3.5.2 Pythia

The event generator Pythia was developed to simulate high-energy particle collision events [41]. An event represents the outcome of a particle collision or decay, and the inherent randomness of quantum processes causes the outcome to vary. An event generator is a numerical algorithm that randomly samples such events repeatedly to build up the expected probability distributions. Its primary focus is effects of quantum chromodynamics (QCD)—interactions mediated by the strong nuclear force. Pythia combines hardcoded physics from theory with phenomenological models whose parameters are tuned to experimental data.

In Pythia, the collisions are modelled using two colliding beams, nevertheless it is possible to model fixed-target experiment by setting the energy of one beam to zero. The default model for simulating heavy-ion collisions is using the `Angantyr` framework, detailed in [41]. Natively, it includes some lighter stable isotopes, accessed through the PDG code 100ZZZAAA0. For example, carbon (1000060120) and aluminium (1000130270) are available by default, as used for on-target DUNE and NOνA, and targetless DUNE respectively. For SHiP, molybdenum and tungsten must be added manually using the `ParticleData::addParticle` command, where the arguments specify the PDG code (100ZZZAAA0), particle name, spin type ($2s+1$), charge type ($3\times$charge), colour type, and nominal mass in GeV [41]. For example, molybdenum can be added through

```
pythia.particleData.addParticle(
    1000420960, "96Mo", 1, 126, 0, 89.334638710673857
);
```

To simulate meson production, the `SoftQCD` process is used. For the 400 GeV proton beam at SHiP, `SoftQCD:inelastic` is used following [7], whilst for the lower 120 GeV beams at DUNE and NOνA, `SoftQCD:all` is recommended [26]. The output is stored in `HepMC` for use with MadDump. The full code is provided in appendix B.

3.6 Statistical Analysis

Constraints on dark matter models are conventionally displayed using exclusion plots, showing which combinations of model parameters are excluded by a null experimental result. This section provides the statistical framework used to produce such plots.

When running an experiment searching for LDM at a proton beam experiment, data are collected and tested for compatibility with a given model [42]. This falsification is performed through hypothesis testing. A certain null hypothesis H_0 is assumed to hold, and the goal is to determine whether the collected data provide sufficient evidence to reject H_0 in favour of an alternative hypothesis H_1. Sufficient here means at some predetermined confidence level CL, often expressed in terms of the significance level α, quantifying the probability of rejecting H_0 when it is in fact true (a type-I error)

$$\mathrm{CL} = 1 - \alpha. \tag{3.7}$$

Following the convention for dark matter searches, a 90% confidence level is used throughout this thesis. The number of observed events $n = b + s$, where b is the expected number of background events and s the expected signal, involves counting events in a given channel, and consequently follows a Poisson distribution

$$n \sim \mathrm{Poisson}(\lambda = b + s). \tag{3.8}$$

The null hypothesis assumes only background is present, giving $\lambda_0 = b$. In other words, it assumes that there are no BSM particles (for this thesis LDM) to measure. The alternative hypothesis posits a BSM signal, giving $\lambda_1 = b + s$. For sufficiently large event counts (a common rule of thumb is $\lambda > 10$), the Poisson distribution is well approximated by a Gaussian

$$n \sim \mathcal{N}(\mu = \lambda, \sigma^2 = \lambda). \tag{3.9}$$

Under the null hypothesis, $\sigma^2 = \lambda_0 = b$. Given the large background counts shown in table 3.2, this approximation is well motivated. The significance can then be evaluated using a one-sided z-test, with H_0: $\mu = \mu_0 = b$ and H_1: $\mu = \mu_1 = b + s > b$. The null hypothesis is rejected at a confidence level $\mathrm{CL} = 1 - \alpha$ if

$$z_\alpha \leq z \equiv \frac{n - \mu_0}{\sigma} = \frac{(b + s) - b}{\sqrt{b}} = \frac{s}{\sqrt{b}}, \tag{3.10}$$

where $z_\alpha = \Phi^{-1}(1 - \alpha)$ and $\Phi(z)$ is the cumulative distribution function (CDF). At 90% CL, $z_{0.1} = 1.282$. Background uncertainties can also be included. Assuming the background consists of different channels i, the total background variance is $\sigma_b^2 = \sum_i (k_i b_i)^2$, where k_i is the fractional uncertainty. The sum runs over

$i \in \{\nu_e, \bar{\nu}_e, \nu_\mu, \bar{\nu}_\mu, \nu_e\text{-CCQE}\}$, with values presented in table 3.2. Including this uncertainty modifies the approximate test statistic to

$$z_\alpha \leq z \equiv \frac{s}{\sqrt{b + \sum_i (k_i b_i)^2}}. \tag{3.11}$$

More sophisticated methods based directly on the Poisson log-likelihood with numerical binning are also possible, but yield similar results for the experiments considered here [26]. Following [7], [26], equation (3.11) is therefore used for simplicity. Fractional uncertainties $k_i = 0.1$, $k_i = 0.05$ and $k_i = 0$ are applied for DUNE, SHiP and NOνA respectively, as in [26].

As discussed in section 2.5.2, exclusion plots are typically displayed in the plane spanned by $y = \epsilon^2 \alpha_D (m_\chi / m_{A'})^4$ and m_χ, with α_D and $m_\chi / m_{A'}$ fixed to benchmark values, leaving ϵ and m_χ as the only free model parameters. For a given combination of ϵ and m_χ, the number of events N can be simulated or computed and compared against the significance criterion in equation (3.11). Plotting the contour of equality divides the parameter plane into an excluded region and an allowed region. Parameter values above the exclusion line would produce a signal large enough to be detected, and can therefore be excluded at $1-\alpha$ confidence level, whilst those below correspond to signals too small to be distinguished from background. The latter means that the experiment is not sensitive enough to exclude the region, and a lower exclusion contour therefore indicates greater experimental sensitivity.

Simulating each point in the parameter plane is computationally expensive. This can be avoided by exploiting the scaling of number of events. As discussed, the number of events at a proton beam experiments scales as $\alpha_D \epsilon^4$, with ϵ^2 from production and $\alpha_D \epsilon^2$ from detection. Simulating N_0 events at a fixed reference ϵ_0, the yield N at an arbitrary ϵ is therefore

$$N = \left(\frac{\epsilon}{\epsilon_0}\right)^4 N_0. \tag{3.12}$$

The simulated signal yield is $s = N$, such that

$$z_\alpha = \frac{N_0}{\sqrt{b + \sum_i (k_i b_i)^2}} \left(\frac{\epsilon_{\text{excl}}}{\epsilon_0}\right)^4 \tag{3.13}$$

Solving for ϵ_{excl} and substituting into y results in

$$y_{\text{excl}} = \epsilon_0^2 \sqrt{\frac{z_\alpha}{N_0}} \left(b + \sum_i (k_i b_i)^2\right)^{1/4} \alpha_D \left(\frac{m_\chi}{m_{A'}}\right)^4. \tag{3.14}$$

One can therefore run the simulation once per m_χ, obtaining N_0 events at a fixed ϵ_0, and then directly compute the exclusion contour. This can be generalised for multiple independent channels. With signal s_j and b_j background in channel j, the total combined test statistic is obtained from summing the square of the individual (Gaussian) channel z-statistic

$$z_\alpha^2 \leq z^2 \equiv \sum_j z_j^2 = \sum_j \frac{s_j^2}{b_j + \sum_i (k_{ij} b_{ij})^2}. \tag{3.15}$$

This approximately follows from the fact that the total likelihood function is the product $\mathcal{L} = \prod_j \mathcal{L}_j$ of each independent channel. The test statistic is then defined from the likelihood ratio

$$\lambda \equiv \frac{\mathcal{L}(\mu)}{\mathcal{L}(\hat{\mu})} = \prod_j \frac{\mathcal{L}_j(\mu)}{\mathcal{L}_j(\hat{\mu})} = \prod_j \lambda_j, \tag{3.16}$$

with $\hat{\mu}$ denoting the maximum likelihood estimator, as

$$q \equiv -2\ln(\lambda) = -2\sum_j \ln \lambda_j = -2\sum_j [l_j(\mu) - l_j(\hat{\mu})] \equiv \sum_j -2\Delta l_j, \tag{3.17}$$

defining the log-likelihood $l \equiv \ln \mathcal{L}$ [42]. Asymptotically, the test statistics is $z \simeq \sqrt{q}$ under Wilks' theorem, leading to the approximate relation $z^2 \simeq \sum_j z_j^2$. The number of events still scales as $N_j = (\epsilon/\epsilon_0)^4 N_{0,j}$, resulting in

$$z_\alpha^2 = \left(\frac{\epsilon_{\text{excl}}}{\epsilon_0}\right)^8 \sum_j \frac{N_{0,j}^2}{b_j + \sum_i (k_{ij} b_{ij})^2}, \tag{3.18}$$

assuming each N_0 is simulated at the same ϵ_0. The combined exclusion contour is

$$y_{\text{excl}} = \epsilon_0^2 \sqrt{z_\alpha} \left(\sum_j \frac{N_{0,j}^2}{b_j + \sum_i (k_{ij} b_{ij})^2}\right)^{-1/4} \alpha_D \left(\frac{m_\chi}{m_{A'}}\right)^4. \tag{3.19}$$

It is straightforward to verify that when b_j, k_{ij}, and $N_{0,j}$ are equal across all channels j, equation (3.19) reduces back to equation (3.14).

4

Secondary Vector Meson Production

This chapter outlines the theoretical framework and analysis used to compute the secondary dark matter production channel: the decays of photoproduced vector mesons into dark matter. Specifically, the photoproduction and subsequent decay of ρ, ω and ϕ mesons are considered. This production channel will sometimes be referred to as invisible vector meson decay, or simply as IVM. In broad terms, IVM consists of the following four parts: production of photons, the photoproduction of vector mesons from said photons, vector meson decay into dark matter, and finally detection of the dark matter. The chapter is structured accordingly.

As a benchmark, the computation is carried out for the older ECN4 configuration of SHiP. In particular, a 400 GeV proton beam colliding with a thick molybdenum target is considered, with dark matter detection taking place in a solid lead detector. Throughout this chapter, SHiP refers exclusively to this older design.

4.1 Photon Production

Unlike the primary production channels—primary meson decay and dark proton bremsstrahlung—this secondary channel cannot be simulated with the previously introduced software. Instead, an analytical approach is adopted. Nevertheless, the number and energy distribution of photons produced at SHiP can be estimated using PYTHIA, where each simulated event constitutes a single proton-molybdenum interaction. The number of photons produced per such interaction is

$$\langle N_\gamma \rangle = \frac{N_\gamma^{\text{sim}}}{N_{\text{events}}}, \tag{4.1}$$

where N_γ^{sim} is the total number of final-state photons from the simulation and N_{events} is the number of simulated events. To obtain the total physical photon yield, the nuclear number density n_{nuc} and total cross section σ_{tot} must be taken into account to include the interaction rate. The depth dependence L is also included by integrating over the interaction probability density as a function of depth x, which follows an exponential attenuation [43]. The various photon production channels present are

accounted for by summing the yield per interaction for each process i, weighted by its probability $\sigma_i/\sigma_{\text{tot}}$. Multiplying with the number of protons on target N_{POT} then gives the total number of produced photons

$$N_\gamma = N_{\text{POT}} \int_0^L n_{\text{nuc}}\sigma_{\text{tot}} \exp(-n_{\text{nuc}}\sigma_{\text{tot}}x)dx \sum_i \frac{\sigma_i}{\sigma_{\text{tot}}} \langle N_\gamma \rangle_i \,. \tag{4.2}$$

The dominant photon production channels at SHiP are soft inelastic QCD processes, direct (prompt) photon production and proton bremsstrahlung. Soft inelastic QCD is dominated by the creation of pseudo-scalar mesons in proton-target collisions, which then rapidly decay to photons. This is of course the Standard Model analogue of the dark meson decays studied in the previous chapter. Precisely as in that case, the leading contributions come from the light neutral pion π^0 and the eta η mesons, with pion decay dominating, primarily due to $\text{BR}(\pi^0 \to 2\gamma) \simeq 98.8\%$ [40].

Direct photon production involves quark-gluon interactions such as $q + g \to q + \gamma$ or $q + \bar{q} \to g + \gamma$. Although the direct photon production yield per interaction $\langle N_\gamma \rangle_{\text{prompt}}$ is sizeable, its cross section is negligible compared to the soft inelastic QCD processes by multiple orders of magnitude, as can be verified by running PYTHIA. The same holds for other hard QCD processes that produce photons secondarily, again predominantly through meson decay, where the mesons are by-products of the various gluon and quark productions.

Proton bremsstrahlung or additional contributions from secondary processes such as electron bremsstrahlung and electron annihilation may also be present. Given the clear dominance of soft inelastic QCD processes, this thesis restricts the analysis to this channel, illustrated in figure 4.1. Secondary cascade effects might also be present. Following [44], these are neglected and left for future study. The resulting photon yield estimate is therefore conservative, though reliable in order of magnitude. The total number of photons with an energy above 100 MeV from the PYTHIA simulation was found to be 3.5×10^{21}, in agreement with [45] within an order of magnitude.

The target of the ECN4 configuration of SHiP, spanning approximately 1.2 m [46], is modelled as solid molybdenum. The nuclear number density is readily computed as $n_{\text{nuc}} = \rho N_A/M$, where ρ is the density, N_A is Avogadro's constant, and M is the molar mass. Simulating the soft inelastic QCD processes in PYTHIA, the total cross section is approximately 1000 mb, giving $n_{\text{nuc}}\sigma_{\text{tot}}L \simeq 7.7$, so the integral in equation (4.2) approaches unity: $1 - \exp(-7.7) \simeq 0.9995$. In other words, the target is optically thick. Although the designed target also contains plates of tungsten, this does not significantly affect the analysis. In any case, the result is compared to the MADDUMP simulated primary channels, which also assumes a solid molybdenum target for ECN4. Acknowledging this, the photon yield at SHiP, equation (4.2), reduces to

$$N_\gamma \simeq N_{\text{POT}} \langle N_\gamma \rangle_{\text{soft}} \,. \tag{4.3}$$

To simulate soft inelastic QCD in PYTHIA, the same `SoftQCD:inelastic` command as in section 3.5.2 is used; the full code of which is provided in appendix B. The simulation is run for $N_{\text{events}} = 10^4$ events and the kinematics of the final-state photons are saved to a `HepMC` file.

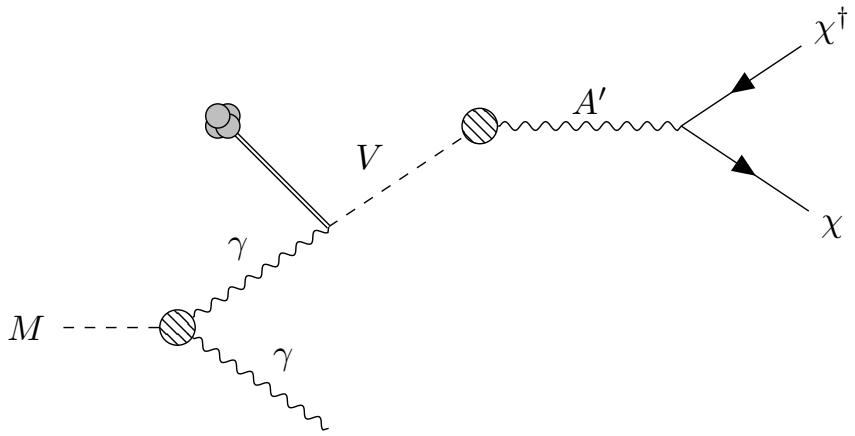

Figure 4.1: Schematic illustration of the secondary invisible vector meson (IVM) production channel with the photon produced via pseudo-scalar meson decay.

4.2 Vector Meson Production

Once produced, a photon may convert into a vector meson in the presence of a nucleus [8]. This is an exclusive forward reaction in which little recoil energy is transferred to the nucleus or nucleons. Specifically, the photoproduction produces vector mesons, since they share the same quantum numbers as the photon, namely $J^{PC} = 1^{--}$. This section presents the method used to estimate the number of these photoproduced vector mesons.

4.2.1 Number of Vector Mesons

The number of vector mesons produced through photoproduction, N_V, may readily be determined from the number of produced photons N_γ and the probability of the exclusive photoproduction p_V

$$N_V = N_\gamma p_V. \tag{4.4}$$

Rather than converting into a vector meson, most photons initiate an electromagnetic shower $\gamma N \to e^+e^-N$ [8]. The probability of photoproduction may therefore be estimated by comparing the two cross sections. The cross section for the electromagnetic shower is approximately

$$\sigma(\gamma N \to e^+e^-N) \simeq \frac{7m_N}{9X_0}, \tag{4.5}$$

where m_N is the recoil nucleus mass and X_0 is the radiation length, conventionally measured in g/cm^2. In comparison to the photon initiated electromagnetic shower, the photoproduction cross section $\sigma_V \equiv \sigma(\gamma N \to VN)$ is minuscule. The probability of photoproduction can therefore be approximated as the ratio

$$p_V \simeq \frac{9X_0}{7m_N}\sigma_V. \tag{4.6}$$

If photoproduction occurs across multiple layers of different material, the number of surviving photons at each point in the material must also be accounted for. This is achieved by weighting by the photon survival probability, giving

$$p_V = \int_0^L \exp\left(-\int_0^x \frac{7\rho(x')}{9X_0(x')}dx'\right)\frac{\rho(x)}{m_N}\sigma_V(x)dx. \tag{4.7}$$

Here, $\rho(x)$ is the local material density and L the total length. In the limit of a thick, uniform target, this reduces back to equation (4.6).

Upon collision of the proton beam with the target, photons and various other particles are produced. The exponential attenuation ensures that all but a negligible fraction of the photons interact well within the target and never escaping it, as intended. At SHiP, the focus is on dark matter and neutrino detection, and all other Standard Model particles are filtered out, either by scattering in the thick target, by the hadron absorber or muon shields. All photoproduced vector mesons can therefore be assumed to originate inside the target.

To illustrate this statement, consider the probability of a photon surviving past the entire uniform target, given by $\mathbb{P}(x) = \exp(-7x/(9X_0))$, where X_0 is expressed in cm. With a radiation length of $X_0 = 0.9593$ cm for molybdenum [40], the target corresponds to roughly $L \sim 125\ X_0$, giving a survival probability of merely $\mathbb{P}(125X_0) \simeq 6 \times 10^{-43}$. It is therefore safe to assume that no photons survive through the target, even if over 3.5×10^{21} photons are produced. Consequently, effectively all interactions occur in the optically thick and uniform target, and the simple expression in equation (4.6) may be used, with X_0, m_N, and σ_V evaluated for molybdenum. The only remaining unknown required to determine N_V is therefore the exclusive photoproduction cross section σ_V.

Photoproduction off a nucleus can proceed through two distinct processes: coherent scattering off the nucleus as a whole, leaving the nucleus in the ground state and with negligible kinetic energy, or incoherent scattering off the individual nucleons [8]. The former dominates at low momentum transfers and is subdominant at higher transfers. Motivated by this, the total cross section is decomposed into two contributions $\sigma_V \equiv \sigma_V^{\text{coh}} + \sigma_V^{\text{inc}}$, which is naturally the integral of the corresponding differential cross section

$$\sigma_V^{\text{coh/inc}} = \int dt \frac{d\sigma_V^{\text{coh/inc}}}{dt}, \tag{4.8}$$

where t is the squared momentum transfer. In the low momentum transfer limit, $|t| \ll m_p^2$, one has $t \simeq -(q_\parallel^2 + q_T^2)$ where

$$q_\parallel = E_\gamma - \sqrt{E_\gamma^2 - m_V^2} \approx \frac{m_V^2}{2E_\gamma}. \tag{4.9}$$

The differential cross section $d\sigma_V^{\text{coh/inc}}$ may be described by a Glauber optical model. Once integrated, photoproduction probability is fully determined, and with it the number of produced vector mesons.

4.2.2 Glauber Optical Model

The Glauber model is a high-energy collision model built on the idea that interactions with a nucleus may be constructed from the scattering amplitudes of the individual nucleons [47]. Central to the model is the eikonal approximation, in which the projectile interacts with the nucleons as it travels a straight line through the nucleus. The model rests on the following assumptions: (i) the nucleons do not move significantly during the collision, (ii) only the nuclear ground state is considered, and (iii) nucleon overlap is negligible, so simultaneous interactions with more than one nucleon can be ignored.

For sufficiently large target nuclei in a high-energy collision, the individual interactions can be replaced by an effective potential. This is the principle of an optical model, named for the similarity between how such collisions behave and how light scatters in a semi-transparent optical medium [48]. Combining these two frameworks results in a Glauber optical model, a well-established model that can accurately describe both coherent and incoherent exclusive photoproduction of vector mesons [8]. An extensive review is given in [47], where a detailed theoretical derivation and comparison with experimental data are provided. For brevity, the relevant formulas are adopted here directly and explained only to the extent necessary to follow the computations. Interested readers are referred to the extensive literature on the subject.

Coherent Photoproduction

For coherent photoproduction, the differential cross section is [8]

$$\frac{d\sigma_V^{\text{coh}}}{dt} = \left.\frac{d\sigma_V^0}{dt}\right|_{\theta=0} \left| \int d^2b dz \; e^{i(\vec{q}_T\cdot\vec{b}+q_\parallel z)} n(b,z) \exp\left(-\beta_V \int_z^\infty dz' n(b,z')\right)\right|^2. \quad (4.10)$$

The first factor is the forward differential cross section off a single nucleon. Experimental data are consistent with an exponential dependence of the angular distribution $d\sigma_V^0 = c\exp(-B|t|)dt$. Accordingly, the forward differential cross section is

$$\sigma_V^0 = \int dt \frac{d\sigma_V^0}{dt} = c\int_0^\infty dt \; e^{-B|t|} = \left.\frac{1}{B}\frac{d\sigma_V^0}{dt}\right|_{t=0} = \left.\frac{1}{B}\frac{d\sigma_V^0}{dt}\right|_{\theta=0}, \quad (4.11)$$

using the fact that $t = 0$ at $\theta = 0$ in accordance with equation (D.8). It also follows immediately that the constant c is equal to $c = B\sigma_V^0$. The parameter B and the individual nucleon photoproduction cross sections σ_V^0 must both be determined experimentally. For B, the values from recent experiments are adopted directly from [8]: $B = 6.4$ GeV^{-2} for ρ, $B = 5.4$ GeV^{-2} for ω, and $B = 3.0$ GeV^{-2} for ϕ. The individual cross sections σ_V^0 are interpolated from the theoretical fit of figure 1 in [49].

Returning to equation (4.10), the incident particle is treated in the centre-of-mass frame and is accordingly described by the impact parameter b and the longitudinal coordinate z along the beam direction. The integrand contains two exponentials: the first accounts for the phase difference arising from photoproduction at different

points in the nucleus, whilst the second accounts for the absorption of the produced meson as it leaves the nucleus. The phase difference depends on the transverse and longitudinal momentum transfer $\vec{q}_T$ and $q_\parallel$, whilst the absorption depends on the parameter β_V defined in terms of the total meson-nucleon scattering cross section σ_{VN} and the real-to-imaginary ratio of the scattering amplitude α_V

$$\beta_V \equiv \frac{\sigma_{VN}}{2}(1 + i\alpha_V). \tag{4.12}$$

For these parameters, Model I in [47] is used, namely

$$\sigma_{\rho N} = \sigma_{\omega N} = 2.08 \left(1 + \frac{0.766}{\sqrt{p}}\right) \text{ fm}^2, \qquad \alpha_\rho = \alpha_\omega = \frac{0.766}{0.766 + \sqrt{p}}, \tag{4.13}$$

whilst for ϕ they are $\sigma_{\phi N} = 1.2$ fm^2, and $\alpha_\phi = 0$. Here, p is the momentum of the forward-produced vector mesons in units of GeV.

Finally, $n(b, z)$ is the nucleon number density distribution. As claimed in [8], the result is not strongly sensitive to its choice. Here, the same distribution—the Woods–Saxon distribution—is adopted

$$n(r) = \frac{n_0}{1 + \exp([r - c]/a)}, \qquad \int d^3r\ n(r) = A, \tag{4.14}$$

where $c = 1.12A^{1/3}$ fm and $a = 0.545$ fm. Motivated by the distribution depending only on the radius $r = \sqrt{b^2 + z^2}$, it is natural to work in cylindrical coordinates. The differential cross section becomes

$$\begin{aligned} \frac{d\sigma_V^{\text{coh}}}{dt} &= B\sigma_0 \left| \int_0^\infty db\ b \int_0^{2\pi} d\phi\ e^{iq_T b\cos\phi} \int_{-\infty}^\infty dz\ e^{iq_\parallel z} n(b,z) e^{-\beta_V T(z,\infty)} \right|^2 \\ &= (2\pi)^2 B\sigma_0 \left| \int_0^\infty db\ bJ_0(q_T b) \int_{-\infty}^\infty dz\ e^{iq_\parallel z} n(b,z) e^{-\beta_V T(z,\infty)} \right|^2, \end{aligned} \tag{4.15}$$

where $J_0(x)$ is the zeroth-order Bessel function of the first kind, and $T(z, \infty) \equiv \int_z^\infty n(b, z')dz'$ is defined for convenience.

The coherent cross section for the ρ meson is shown as a function of momentum transfer $|t|$ by the dashed lines in figure 4.2, computed for two benchmark photon energies E_γ. Comparison with the incoherent cross section, represented by the solid lines, confirms the previous statement of coherent scattering dominating at low momentum transfer.

Incoherent Photoproduction

The differential cross section for incoherent photoproduction is given by [8]

$$\begin{aligned} \frac{d\sigma_V^{\text{inc}}}{dt} &= \frac{d\sigma_0}{dt} \int d^2b\ dz\ n(b,z) \exp\left(-\sigma_{VN} \int_z^\infty dz' n(b,z')\right) \\ &\quad \times \left| 1 - \int_{-\infty}^z dz''\ n(b,z'') \beta_V e^{iq_\parallel (z''-z)} \exp\left(-\beta_V \int_{z''}^z dz'''\ n(b,z''')\right) \right|^2. \end{aligned} \tag{4.16}$$

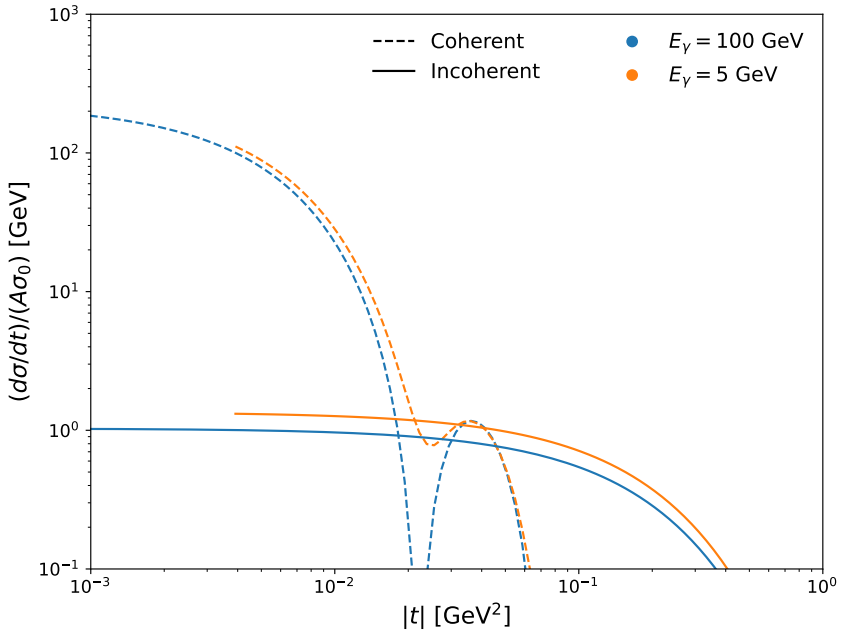

Figure 4.2: Illustration of the differential cross section for coherent (dashed) and incoherent (solid) photoproduction of the ρ meson at two benchmark photon energies. Shown as a function of the momentum transfer $|t|$ and normalised to the sum of the individual nucleon cross sections.

The first exponential accounts for absorption, whilst the final factor is a shadowing correction. It encodes the phenomenon of destructive interference between photoproduction occurring directly at z and photoproduction occurring at an earlier point z'' followed by scattering at z. Rewriting the expression in cylindrical coordinates gives

$$\begin{aligned}\frac{d\sigma_V^{\text{inc}}}{dt} &= 2\pi B\sigma_V^0 e^{-B|t|}\int_0^\infty db\, b\int_{-\infty}^{\infty} dz\; n(b,z)e^{-\sigma_{VN}T(z,\infty)} \\ &\times\left|1-\int_{-\infty}^{z} dz''\; n(b,z'')\beta_V e^{iq_\parallel(z''-z)}e^{\beta_V T(z'',z)}\right|^2 .\end{aligned} \tag{4.17}$$

Total Cross Section

The total cross section $\sigma_V = \sigma_V^{\text{coh}} + \sigma_V^{\text{inc}}$ is shown as a function of photon energy in figure 4.3 for the three vector mesons considered: ρ, ω and ϕ. At high photon energies, the total cross section is approximately equal to the sum of the individual nucleon cross sections.

A minimum photon energy is required for any photoproduction to occur, and this threshold differs between the coherent and incoherent cases. A straightforward application of four-momentum conservation gives that the minimum energy is

$$E_{\gamma,\min}^V = m_V + \frac{m_V^2}{2m_X}. \tag{4.18}$$

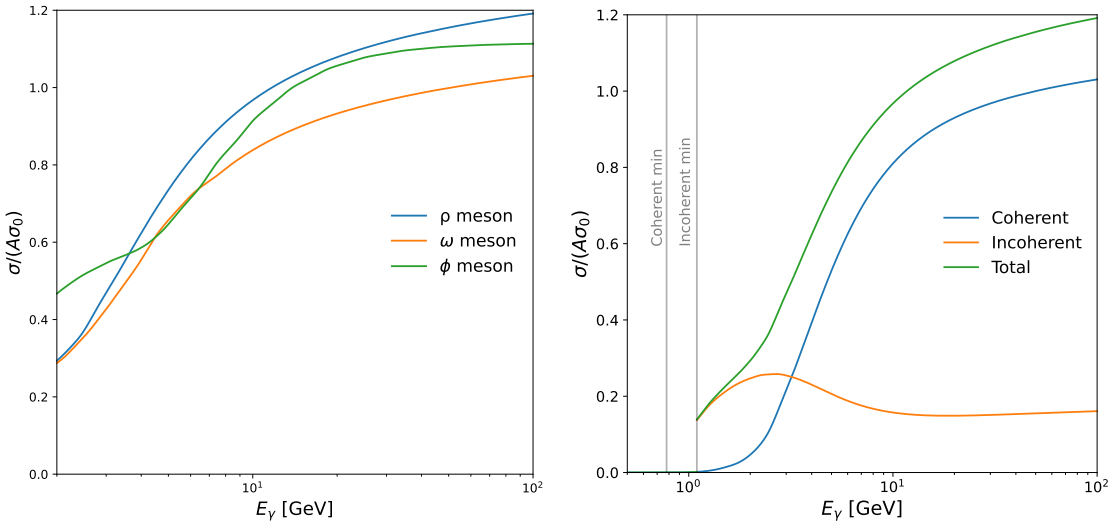

(a) **(b)**

Figure 4.3: Total cross section, normalised to the sum of the individual nucleon cross sections, as a function of photon energy. In (a), the cross section is shown for the ρ, ω and ϕ mesons, whilst (b) shows only the ρ meson, decomposed into coherent and incoherent contributions and indicating their respective minimum energy thresholds.

For coherent production, the photon scatters off the entire nucleus such that $m_X = M$ is the mass of the nucleus. In contrast, for incoherent production $m_X = m_n$ with m_n being the individual nucleon mass. Consequently, the minimum energy necessary for incoherent photoproduction is higher.

4.3 Dark Matter Production

After being produced, a vector meson decays rapidly before interacting with any nuclei in the target [8]. Through kinetic mixing, some fraction of the vector mesons converts to a dark photon, which subsequently either decays visibly into Standard Model particles or decay invisibly into dark matter, as discussed in the context of the primary channels [15]. As before, the relevant parameter region permits the assumption $\mathrm{BR}(A' \to \chi\bar{\chi}) \simeq 1$. Consequently, the photoproduced vector mesons have a well-defined decay channel to dark matter through the dark photon. The produced dark matter is then able to escape the target to the detector and potentially be detected.

The expected number of dark matter particles produced equals the number of produced vector mesons N_V times the branching ratio for an on-shell vector meson V to decay into a dark matter pair $\chi\chi^\dagger$ through a virtual dark photon A'

$$N_\chi = N_V \mathrm{BR}(V \to \chi\chi^\dagger). \tag{4.19}$$

Since the kinetic mixing is rather small, $\epsilon \ll 1$, the decay rate into dark matter is

tiny compared to ordinary Standard Model particles. Consequently,

$$\mathrm{BR}(V \to \chi\chi^\dagger) = \frac{\Gamma(V \to \chi\chi^\dagger)}{\Gamma_{\mathrm{tot}}} \simeq \frac{\Gamma(V \to \chi\chi^\dagger)}{\Gamma(V \to \mathrm{SM})}, \tag{4.20}$$

where the decay widths to Standard Model particles are $\Gamma(\rho \to \mathrm{SM}) = 147.4$ MeV, $\Gamma(\omega \to \mathrm{SM}) = 8.68$ MeV and $\Gamma(\phi \to \mathrm{SM}) = 4.249$ MeV [40].

The decay rate into dark matter through a dark photon is computed using the standard Feynman rules. From the Lagrangian, equation (2.9), the relevant interaction terms for the dark sector are

$$\mathscr{L} \supset e\epsilon A'_\mu J^\mu_{\mathrm{em}} + A'_\mu J^\mu_\chi. \tag{4.21}$$

The corresponding Feynman diagram is illustrated in figure 4.4. The vector meson to dark photon conversion is most conveniently described as an effective vertex characterised by a form factor f_V. The form factor is defined by the matrix element $\langle 0|J^\mu_{\mathrm{em}}|V(\epsilon)\rangle = im_V f_V \epsilon^\mu$, which encodes the amplitude for the electromagnetic current to create a vector meson from the vacuum. The contribution from this vertex is therefore $\epsilon e i m_V f_V \epsilon^\mu$. Given the form of the electromagnetic current $J^\mu_{\mathrm{em}} = \sum_q Q_q \bar{q}\gamma^\mu q$, the form factor is $f_V = \sum_q Q_q f_V^q$. Using the values listed in [8], one finds $f_\rho = 154$ MeV, $f_\omega = 46$ MeV and $f_\phi = -75$ MeV.

The remaining Feynman diagram contributions are straightforward. The virtual dark photon is a massive spin-1 propagator, contributing $-i(\eta^{\mu\nu} - q^\mu q^\nu/m^2_{A'})/(q^2 - m^2_{A'})$. The dark matter couples to the dark photon with strength g_D; for a complex scalar dark matter, the vertex factor then becomes $g_D(p - p')^\nu$, where p and p' are the four-momenta of the complex scalar χ and its complex conjugate $\chi^\dagger$ respectively. The full Feynman amplitude is therefore

$$\mathcal{M} = \epsilon e m_V f_V \epsilon_\mu \frac{\eta^{\mu\nu} - q^\mu q^\nu/m^2_{A'}}{q^2 - m^2_{A'}} g_D (p - p')_\nu, \tag{4.22}$$

where q^μ denotes the incoming vector meson momentum. Squaring and averaging over polarisations yields the decay width

$$\Gamma(V \to \chi\chi^\dagger) = \frac{\alpha_D (\epsilon e)^2 f_V^2}{12} \frac{(m_V^2 - 4m_\chi^2)^{3/2}}{(m^2_{A'} - m_V^2)^2 + m^2_{A'}\Gamma^2_{A'}}, \tag{4.23}$$

the full derivation is provided in appendix C. The denominator contains the decay width for the dark photon to dark matter $\Gamma_{A'}$, given by [8]

$$\Gamma_{A'} = m_{A'} \frac{\alpha_D}{12} \left(1 - \frac{4m_\chi^2}{m^2_{A'}}\right)^{3/2}. \tag{4.24}$$

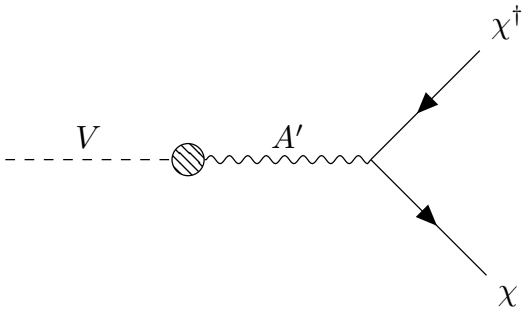

Figure 4.4: Feynman diagram for vector meson V decay into dark matter pair $\chi\chi^\dagger$ through kinetic mixing with a virtual dark photon A'.

4.4 Dark Matter Detection

Not all produced dark matter particles are detected. As established, direct detection fixed-target experiments such as SHiP have three detection channels: (i) elastic scattering off electrons, (ii) elastic scattering off nucleons in the nuclei, and (iii) deep inelastic scattering (DIS) off quarks in the nuclei [7].

The number of signal events N_{sig} depends not only on the number of produced dark matter particles N_χ, but also on the detection efficiency ϵ_{eff}, the detector length L, the scattering cross section σ_X for each detection channel, and the number density n_X of target particles. Altogether, the expected number of signal events is

$$N_{\text{sig}} = \epsilon_{\text{eff}} L \sum_X \left[n_X \sum_i \sigma_X(E_i) \right]. \tag{4.25}$$

The outer sum runs over the detection channels $X \in \{e, N, \text{DIS}\}$ and the inner sum runs over all the N_χ individual dark matter particles, with incoming energy E_i. In accordance with [50], the efficiency at SHiP is taken to be $\epsilon_{\text{eff}} = 0.5$. The number density is computed as

$$n_X = \frac{\rho}{M} N_A f_X, \tag{4.26}$$

where ρ is the detector density, M its molar mass, N_A is Avogadro's constant and $f_e = Z$, and $f_N = f_{\text{DIS}} = A$, with Z denoting the proton number and A the nucleon number.

4.4.1 Elastic Electron Scattering

The differential cross section in the laboratory frame for dark matter with incoming energy E scattering off an electron, producing a final-state electron with energy E_k is [51]

$$\frac{d\sigma_e}{dE_k} = 4\pi\epsilon^2\alpha_D\alpha \frac{2m_e E^2 - (E_k - m_e) f(E, E_k)}{(E^2 - m_\chi^2)(m_{A'}^2 + 2m_e(E_k - m_e))^2}. \tag{4.27}$$

Here, $f(E, E_k)$ is a model dependent factor, which for complex scalar dark matter takes the form

$$f(E, E_k) = 2m_e E + m_\chi^2. \tag{4.28}$$

The total cross section is obtained by integrating over the final electron energies E_k

$$\sigma_e = \int_{E_k^{\min}}^{E_k^{\max}} dE_k \frac{d\sigma_e}{dE_k}. \tag{4.29}$$

The integration limits $E_k^{\min}$ and $E_k^{\max}$ are set by both the experimental detection window and the kinematics of elastic two-body scattering. For SHiP, the optimal window for recoil electron detection is once again taken to be $E_k^{\min} = 1$ GeV and $E_k^{\max} = 5$ GeV, as determined in [7]. The kinematically valid region, derived in appendix D, is

$$m_\chi < E, \qquad E_k \leq m_e + \frac{2m_e(E^2 - m_\chi^2)}{m_e^2 + m_\chi^2 + 2m_e E}, \tag{4.30}$$

4.4.2 Elastic Nucleon Scattering

Elastic scattering off a nucleon $N = p, n$ in the laboratory frame is described by the differential cross section [51]

$$\frac{d\sigma_N}{dE_\chi} = 4\pi\epsilon^2\alpha_D\alpha \frac{F_{1,N}^2 A(E, E_\chi) + F_{2,N}^2 B(E, E_\chi) + F_{1,N}F_{2,N}C(E, E_\chi)}{(E^2 - m_\chi^2)(m_{A'}^2 + 2m_N(E - E_\chi))^2}, \tag{4.31}$$

where E (E_χ) is the incoming (outgoing) dark matter particle energy such that the momentum transfer is $Q^2 = 2m_N(E - E_\chi)$. The functions A, B, C are model dependent. For complex scalar dark matter, they are

$$\begin{aligned} A &= E_\chi(2Em_N + m_\chi^2) - Em_\chi^2, \\ B &= \frac{1}{4}\left(E - E_\chi\right)\left[E^2 + 2(E + m_N)E_\chi + E_\chi^2 - 2Em_N - 4m_\chi^2\right], \\ C &= -(E - E_\chi)\left[m_N(E - E_\chi) + 2m_\chi^2\right]. \end{aligned} \tag{4.32}$$

Finally, $F_{1,N}$ and $F_{2,N}$ are nucleon form factors given by

$$F_{1,N} = \frac{q_N}{(1 + Q^2/m_N^2)}, \qquad F_{2,N} = \frac{\kappa_N}{(1 + Q^2/m_N^2)}, \tag{4.33}$$

with $q_p = 1$, $\kappa_p = 1.79$ for the proton, while $q_n = 0$, $\kappa_n = -1.9$ for the neutron [52]. Integrating the differential cross section gives the total cross section

$$\sigma_N = \int_{E_\chi^{\min}}^{E_\chi^{\max}} dE_\chi \frac{d\sigma_N}{dE_\chi}.$$

The integration limits are obtained from the kinematically allowed range. Including a minimum nucleon recoil energy for detection $E_{\text{cut}} = 1$ GeV at SHiP [53], the valid range of outgoing dark matter energies is

$$E - \frac{2m_N(E^2 - m_\chi^2)}{m_\chi^2 + m_N^2 + 2m_N E} \leq E_\chi \leq E + m_N - E_{\text{cut}}, \tag{4.34}$$

as derived in appendix D. The cross section used in equation (4.25) is the effective elastic nucleon cross section

$$\sigma_N^{\text{eff}} = \frac{1}{A}\left[Z\sigma_p + (A-Z)\sigma_n\right]. \tag{4.35}$$

4.4.3 Deep Inelastic Scattering

Deep inelastic scattering off nuclei is described by the differential cross section

$$\frac{d\sigma_{\text{DIS}}}{d\nu dQ^2} = \frac{\pi\epsilon^2\alpha_D\alpha}{E^2 - m_\chi^2}\frac{\nu}{(Q^2+m_{A'}^2)^2}\left[\frac{(2E-\nu)^2}{\nu^2+Q^2} - \frac{Q^2+4m_\chi^2}{Q^2}\right]F(x_{\text{bj}}, Q^2), \tag{4.36}$$

as derived in appendix E. Here, E is the incoming dark matter energy, $Q^2 = -(p-p_\chi)^2$ is the squared momentum transfer with p and p_χ as the incoming and outgoing dark matter four-momenta, and ν is the energy of the mediating dark photon A' in the nucleus rest frame. Finally, $F(x_{\text{bj}}, Q^2)$ is the sum of parton distribution functions (PDFs) over quark flavours, assuming the mediator couples equally to each

$$F(x_{\text{bj}}, Q^2) \equiv \sum_q x_{\text{bj}} f_{q/A}(x_{\text{bj}}, Q^2), \tag{4.37}$$

where x_{bj} is the Bjorken scaling variable

$$x_{\text{bj}} = \frac{Q^2}{2M\nu}, \tag{4.38}$$

with $M \simeq Am_p$ now denoting the mass of the detector nucleus. The sum runs over $q \in \{d, u, s, \bar{d}, \bar{u}, \bar{s}\}$, neglecting the insignificant contributions from b, $\bar{b}$, c, and $\bar{c}$ quarks. The nuclear parton distribution functions may either be supplied directly for a nucleus, or otherwise approximated from the proton PDFs

$$f_{q/A}(x_{\text{bj}}, Q^2) \simeq Zf_{q/p}(x_{\text{bj}}, Q^2) + (A-Z)f_{q/n}(x_{\text{bj}}, Q^2). \tag{4.39}$$

The neutron PDFs $f_{q/n}$ are related to the proton PDFs $f_{q/p}$ by assuming isospin symmetry, under which $u \leftrightarrow d$ [54].

This thesis uses nuclear parton distribution functions. In particular, the SHiP ECN4 detector is made of lead, such that the `EPPS16nlo_CT14nlo_Pb208`[1] parton distribution is used, including nuclear modifications supplied by [54] to the next-to-leading order proton parton distribution function from [55]. Although SHiP specifies ^{207}Pb, this was deemed to be a more accurate alternative to the lack of ^{207}Pb parton distribution functions compared to the approximation built from proton PDFs, excluding nuclear effects. Nevertheless, these differences are small, of the order of a few percent.

The total cross section is

$$\sigma_{\text{DIS}} = \int d\nu \int dQ^2 \frac{d\sigma_{\text{DIS}}}{d\nu dQ^2}, \tag{4.40}$$

[1]Available at https://www.lhapdf.org/pdfsets.html.

with $Q^2_{\text{cut}} < Q^2 < 2M\nu$, ensuring $0 \leq x_{\text{bj}} < 1$. The limits for ν are $E^{\nu}_{\text{cut}} < \nu < E - m_{\chi}$. Following [56], $E^{\nu}_{\text{cut}} = 20$ GeV. For deep inelastic scattering to occur, Q^2 must be large enough for the dark matter particle to interact with the individual quarks and gluons. Moreover, the computed approximate differential cross section is valid as long as Q^2 is larger than a few GeV^2. Consistent with [50], $Q^2_{\text{cut}} = 2$ GeV^2 is therefore imposed.

5

Results

In this chapter, the results are presented and discussed. It starts with a section on the sensitivity results for the three proton beam experiments considered from the simulations using PYTHIA and MADDUMP. Thereafter, a section is dedicated to presenting and discussing the results of the new secondary meson decay channel.

5.1 Sensitivity of Proton Beam Experiments

Figure 5.1 shows the simulation results for both the old ECN4 and new ECN3 proposed layout of SHiP. In particular, figure 5.1a shows the signal events at fixed ϵ, whilst 5.1b shows the sensitivity at 90% CL. Both plots only consider the dominant elastic electron scattering detection channel. The dominance of the meson decays, especially that of pion decay, is easily seen for the lower mass regime. The resonance peak of the proton bremsstrahlung caused by including the effect of mixing with ρ and ω mesons is also clearly visible.

The results for ECN4 and ECN3 are very similar. Having a longer duration time of 15 years instead of 5 years, ECN3 naturally has more signal events, although perhaps not as much as one naively might guess. The run time is three times longer, and the target change from molybdenum to the denser tungsten leads approximately to twice as many mesons produced, but the detector size, distance, and material were also changed. The sensitivity is even more similar, since the increase in operation time also comes with an increase in background events. The background for ECN4 was assumed to scale linearly with operation time. This further affects the sensitivity, not only by increasing the background but also by increasing the background uncertainty. In reality, the updated design changes might decrease the (yearly) background and its fractional uncertainty. The similar sensitivities indicate that previous studies conducted using the old ECN4 design are still roughly valid, and that choosing the, arguably simpler, ECN4 design alternative for studies is still sensible. Further, more detailed studies of the background at the new facility are required for a more accurate result.

The 90% CL sensitivity for DUNE configured in beam dump (targetless) mode considering only elastic electron scattering is presented in figure 5.2. Compared to

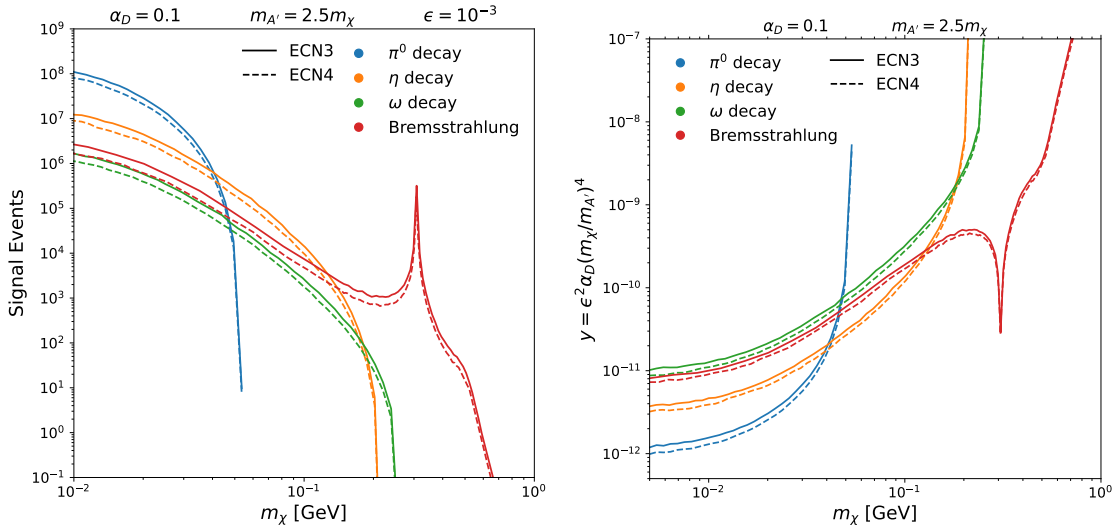

(a) **(b)**

Figure 5.1: Simulated (a) signal event counts for a benchmark value $\epsilon = 10^{-3}$, and (b) 90% CL exclusion limits for the old ECN4 design (dashed line) and the new ECN3 design (solid line) of SHiP, obtained using MadDump. The contributions from the production channels—π^0 decay (blue), η decay (orange), ω decay (green), and proton bremsstrahlung (red)—are shown individually.

the previous SHiP sensitivity, DUNE has higher sensitivity with about an order of magnitude. This is likely due to its higher POT, but can also be affected by the other design differences. However, it is important to keep in mind that the beam dump is assumed to run for seven years, perhaps somewhat optimistic given it would hinder its primary neutrino program. Nevertheless, it displays DUNE's great potential in contributing to LDM searches.

A comparison of the 90% CL sensitivity of the three proton beam experiments is shown in 5.3, considering once again only detection through electron scattering. The blue line represents the combined sensitivity of π^0, η, and ω decay, and proton bremsstrahlung for SHiP ECN3. The three different modes—target (on-axis), beam dump (targetless), and PRISM (off-axis)—are displayed for DUNE in orange, green and red. It is assumed for all three modes that half the time is run in the neutrino mode, and half in the antineutrino mode. DUNE PRISM is run with equal time allocations at 0, 6, 12, 18, 24 m off-axis during the 7 years run. For target and beam dump, the sensitivity includes the same channels as SHiP. For PRISM, only the π^0 decay and bremsstrahlung are included, since the number of events for the other channels were too few to accurately simulate without great computation costs. Their contributions would nonetheless be negligible, as can be inferred from figure 5.1b and 5.2. Likewise, the result for NOνA also only includes π^0 decay and bremsstrahlung. Figure 5.3 reveals the improvements in sensitivity of operating either the targetless mode or using the PRISM mechanism. Although the targetless mode sees a much larger improvement, the off-axis configuration also improves the sensitivity slightly. Including additional off-axis positions is expected to further increase the sensitivity.

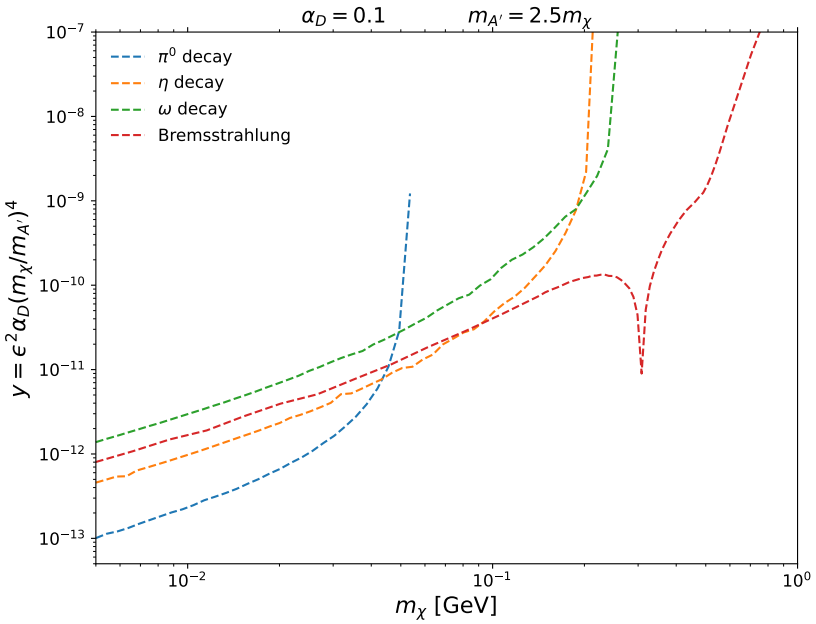

Figure 5.2: Simulated 90% CL exclusion limits for DUNE operating in beam dump (targetless) mode using MadDump, assuming a 7-year run. The contributions from the production channels—π^0 decay (blue), η decay (orange), ω decay (green), and proton bremsstrahlung (red)—are shown individually.

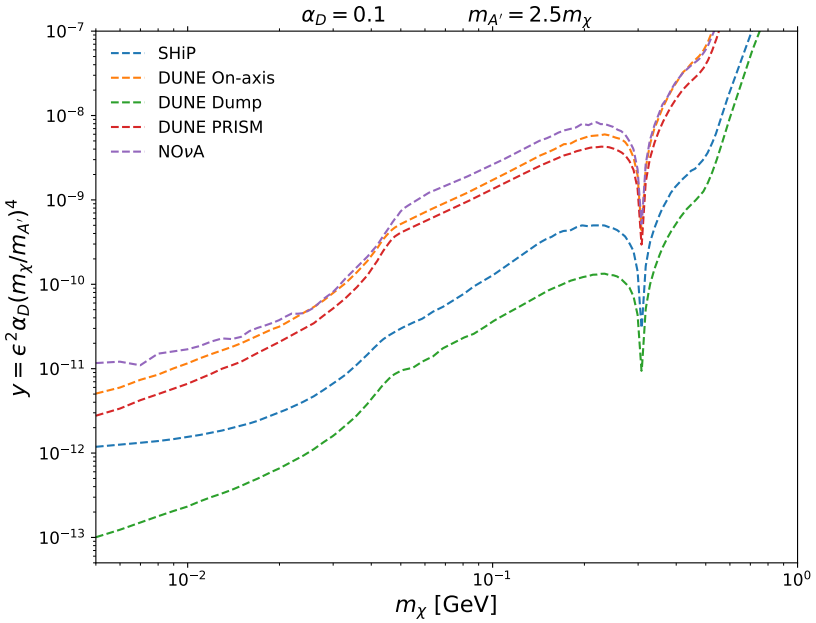

Figure 5.3: Comparison of 90% CL exclusion bounds for the new ECN3 design of SHiP (blue), three operating modes of DUNE: on-axis (orange), beam dump (green), and PRISM (red) up to 24 m off-axis, and NOνA. SHiP, DUNE beam dump and on-axis shows combined contributions of π^0, η decay, ω decay and proton bremsstrahlung. DUNE PRISM and NOνA only include π^0 decay and proton bremsstrahlung.

5.2 Secondary Vector Meson Production

The energy and momentum distributions of the produced photons at the old ECN4 design of SHiP as simulated in PYTHIA is presented in figure 5.4. Not surprisingly, the transverse momentum is approximately Gaussian around zero momentum. The energy spans the interval from below 1 MeV up to almost 300 GeV. However, the mean is only 4.8 GeV, such that most produced photons are rather low energy.

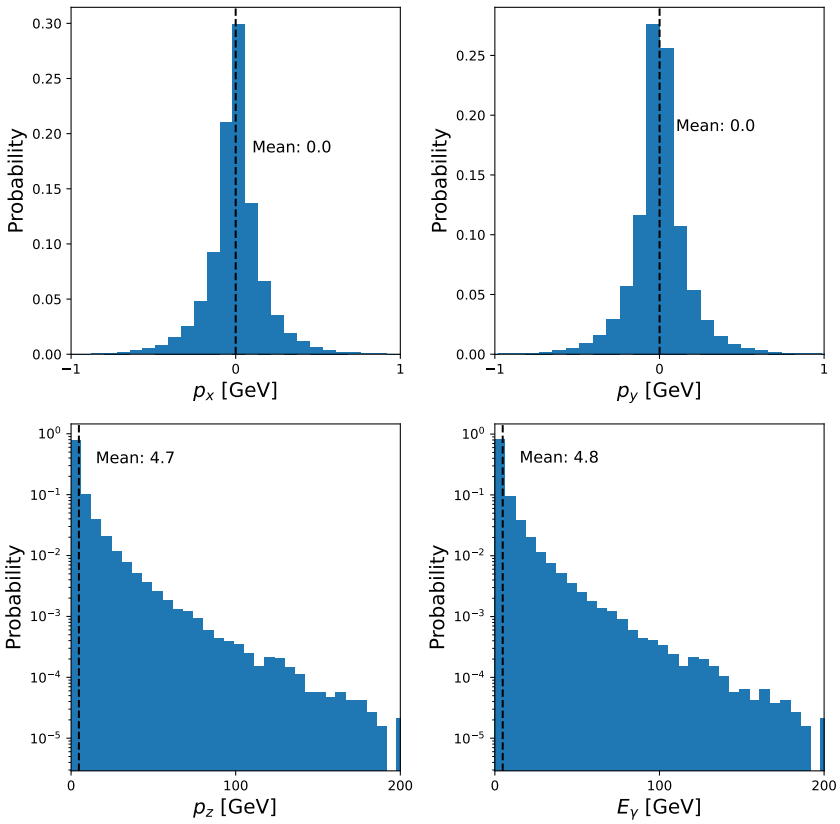

Figure 5.4: Momentum and energy distributions of the produced photons at the ECN4 configuration of SHiP simulated using PYTHIA with the flag `SoftQCD:inelastic`. Vertical black dashed line indicate the mean momentum or energy. Note that y-axis is logarithmic in the lower panels.

In figure 5.5, the 90% CL exclusions for the secondary invisible vector meson (IVM) decay channel are displayed, as computed in chapter 4. It shows the three modes of detection: elastic electron scattering (blue), elastic nucleon scattering (orange) and deep inelastic scattering (green). Whilst, elastic electron scattering indeed dominates at lower masses, nucleon scattering becomes dominant at higher masses. The sensitivity for the nucleon scattering and DIS is however less precisely determined, since the electron background is far more well studied than the other two, and because in this thesis the background for nucleon scattering was assumed to be the same as for DIS.

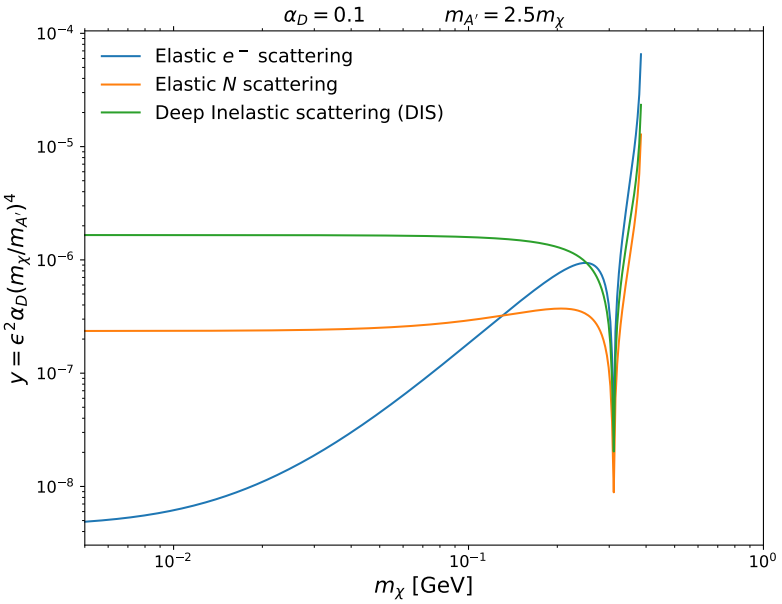

Figure 5.5: 90% CL exclusion bounds on the new secondary vector meson production channel in which photoproduced vector mesons decay into dark matter via a dark photon mediator. The sensitivity is shown separately for the three detection modes: elastic scattering off electrons (blue), elastic scattering off nucleons (orange), and deep inelastic scattering (green).

A comparison between the secondary invisible vector meson decay and the proton bremsstrahlung, figure 5.6, reveal a large difference in number of signal events and consequently also sensitivity at 90 % CL. The figure shows secondary IVM for the ρ, ω and ϕ meson and includes only detection from elastic electron scattering.

Contrary to electron beam experiments where the secondary IVM enhances the sensitivity at higher masses compared to the bremsstrahlung, this is not the case at the proton beam dump SHiP. Electrons are elementary particles with no hadronic substructure, and therefore do not exhibit any intrinsic resonant coupling to vector mesons. As a result, dark bremsstrahlung at electron experiments shows no resonance at the ρ and ω meson masses. Thus, in this region, the secondary IVM are more sensitive. In proton experiments such resonance enhancements are present thanks to the proton structure. Nevertheless, it might be expected that the secondary IVM could at least extend the peak or otherwise enhance the sensitivity in certain regions due to the increased photon production from meson decay. This is however not observed in practice.

Not only does the secondary IVM channel fail to increase the sensitivity, the difference relative to the proton bremsstrahlung is also significant. Throughout the computation, various approximations were performed. Some of these, such as assuming only forward scattering and no kinematic cuts on the detection angle, slightly overestimate the number of detections. Others, such as including only soft QCD production of photons whilst excluding any secondary productions, instead provide a more conservative

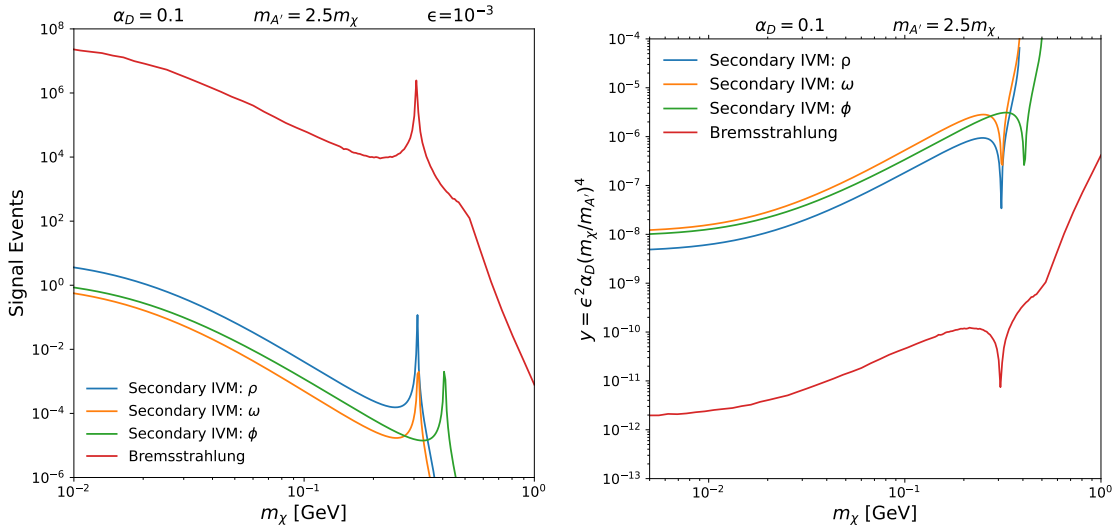

(a) **(b)**

Figure 5.6: Comparison of (a) signal event count, (b) 90% exclusion bounds of the new secondary invisible vector meson (IVM) decay channel, with dark bremsstrahlung at ECN4 configuration of SHiP, for ρ (blue), ω (orange), and ϕ (green) mesons. Only the dominant elastic electron scattering detection channel is included.

estimation. Restricting the analysis to soft QCD is the largest potential suppression. Although prompt photon production proved insignificant, additional photons could potentially arise from ordinary electromagnetic proton bremsstrahlung. Indeed, it was the analogous electron bremsstrahlung which was considered in the paper [8]. As was argued in section 4.1, however, the order of magnitude of photons produced in this analysis agrees with previous estimates. Thus, even if including proton bremsstrahlung would increase the number of photons, an increase within the order of magnitude would still be insufficient to explain roughly the three orders of magnitude difference in sensitivity (corresponding to approximately six orders of magnitudes in the number of detected events).

A caveat to the former claim is nonetheless worth mentioning. Figure 4.3 shows that the total cross section (and by equation (4.6) therefore also the probability of photoproduction) increases with photon energy. Meanwhile, the energy distribution in figure 5.4 reveals that the mean energy is only 4.8 GeV, and most photons have energies below 10 GeV. Although the inclusion of additional production channels may not significantly increase the total photon yield, the effect would be larger if those channels would favour higher-energy photons. Moreover, higher-energy photons would produce more energetic dark matter particles, thereby increasing the detection too. This effect is illustrated in figure 5.7. The figure compares the previous estimated signal events for the ρ meson (blue) with two benchmark scenarios in which all photons are instead assigned fixed energies of either $E_\gamma = 7$ GeV (orange) or $E_\gamma = 300$ GeV (green). The lower-energetic scenario does not even manage to detect enough events for higher dark matter masses, having too little energy to produce

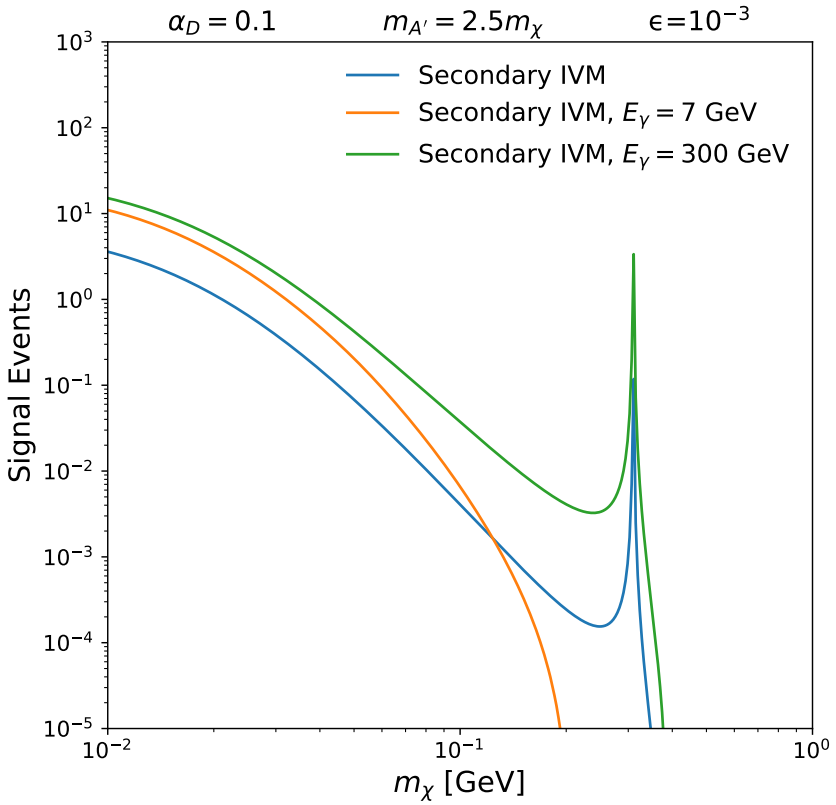

Figure 5.7: Signal event counts for a benchmark value of $\epsilon = 10^{-3}$ for the new secondary invisible vector meson (IVM) decay channel as simulated in the ECN4 configuration of SHiP (blue), and compared to two benchmark scenarios with fixed photon energies at $E_\gamma = 7$ GeV (orange) and $E_\gamma = 300$ GeV (green).

detectable scattering events. Increasing the photon energy does indeed increase the estimated signal events. Still, the enhancement remains far too small to close the large sensitivity gap relative to proton bremsstrahlung even for the more extreme $E_\gamma = 300$ GeV scenario.

A more plausible explanation is the fact that the increase in the number of ordinary photons produced, relative to the number of dark photons produced through proton bremsstrahlung, is more than compensated for by the suppression arising from both the probability of a vector meson being photoproduced and the branching ratio of said vector meson to decay into dark matter. In fact, a back-of-the-envelope estimate can demonstrate this. The PYTHIA simulation produced approximately $\mathcal{O}(10^{21})$ photons with energies sufficiently large for photoproduction to ρ for the full 2×10^{20} POT. Approximating $\sigma \sim A\sigma_0$ at the order of magnitude according to figure 4.3, the probability of a photon to undergo photoproduction is roughly 10^{-4} according to equation (4.6), where $X_0 \sim 10$ g/cm^2 and $\sigma_0 \sim 10$ μb. Using $m_\chi = 10$ MeV and $\epsilon = 10^{-3}$ as benchmark values, then $\mathrm{BR}(V \to \chi\chi^\dagger) \sim 10^{-10}$. Likewise, $Ln_e\sigma_e \sim 10^{-7}$. Altogether, the expected signal is of order $N_{\mathrm{sig}} \sim 10^0$–$10^1$, in reasonable agreement with figure 5.6a for the ρ meson. This means that the

combined suppression for photoproduction and decay to dark matter is approximately of order $10^{-4} \times 10^{-10} \sim 10^{-14}$. To achieve sensitivity comparable to ordinary proton bremsstrahlung, it is therefore necessary for there to be around 10^{14} more ordinary photons produced than dark photons. However, estimating backwards from 10^7 signal events as seen for $m_\chi = 10$ MeV in figure 5.6a, the number of produced dark photons is around 10^{14}, only around 10^7 fewer dark photons than ordinary photons.

The large overall suppression factor of order 10^{-14} therefore makes it unlikely that any inclusion of additional photon production channels, even those with possibly more high-energy photons, could sufficiently compensate the discrepancy. This, however, raises the question of why such suppression is not observed for the electron beam. Although the proton beam needs direct detection, strongly suppressing the number of detected events compared to electron beam experiments, both dark bremsstrahlung and the secondary IVM channel at proton beam experiments are affected by this suppression. Comparing the four steps of producing photons, vector meson photoproduction, vector meson decay into dark matter, and dark matter detection, electron beam experiments differ only in the first and last steps. Since the detection affects dark bremsstrahlung and secondary IVM within each experiment similarly, a relative comparison should cancel its effect. One could again argue about energy differences (and possibly differences in kinematic cut), however these should still be small compared to the observed order of magnitude differences. The remaining difference should therefore originate primarily from the production of photons. Indeed, the original motivation for the thesis was the expectation that proton beam experiments should favour secondary IVM due to having further photon production channels compared to electron beam experiments.

One possible explanation could be that there is something fundamental at proton beam experiments decreasing the ratio of photon production compared to dark photon production from bremsstrahlung. However, by the previous argument of additional photon production channels, this explanation is not entirely convincing. Another explanation is that the dark photon production is overestimated in the simulation within MadDump, or alternatively that the dark photon production from electron bremsstrahlung is underestimated. Of these two possibilities, the former seems more likely. Proton bremsstrahlung is still in the development version of the code, and it relies on simplified proton-on-proton collision models, not taking the material of the target into consideration. Nevertheless, the implementation has been used in previous publications, for example [7].

The remaining question is therefore why the ratio of ordinary photon production to dark photon production from bremsstrahlung is sufficiently large to compensate for the effect of photoproduction probability and branching ratio suppression for electron beam experiments but not for proton beam experiments. No fully satisfactory explanation has yet been identified, and would require further investigation to unravel. Some explanations have been put forward here, most of which can likely be excluded or appear insufficient to explain the full magnitude of the discrepancy.

6

Conclusion

Light dark matter (LDM) serves as a compelling new dark matter candidate, opening up the possibility of detection at proton beam experiments. With the development of new proton fixed-target experiments both dedicated, and adaptable for, LDM searches, new regions of the parameter space may be explored. In this thesis, the sensitivity at two upcoming experiments, SHiP and DUNE ND, has been simulated, showing increases in sensitivity compared to the existing NOνA ND experiment. The updated SHiP design was shown to slightly decrease the sensitivity, although the difference was modest. For a more precise comparison, a dedicated detailed study of the background at the new facility is needed. The upcoming DUNE ND experiment slightly improves the sensitivity compared to the existing NOνA experiments, and by operating in off-axis modes made possible by the PRISM mechanism, the sensitivity may be increased further. The largest increase in sensitivity was, however, seen when removing the target and operating DUNE ND as a beam dump. Then, DUNE ND can explore regions even beyond SHiP. Although this will hinder the intended neutrino searches, it nevertheless motivates consideration of such operation. A detailed study of the background and sensitivity for the three possible operational modes at DUNE ND including the phase II strategy would be a natural and interesting extension of this work.

In addition to the primary dark matter production channels, a new secondary channel was considered. This channel consists of photoproduced vector mesons decaying to dark matter. Although the sensitivity has been shown to increase at electron beam experiments, no such increase was shown for proton beams. This discrepancy is somewhat unexpected. In particular, proton beam experiments allow additional photons to be produced through meson decay not present in electron beam experiments. Nevertheless, this increased photon production proved to be counteracted by the probability of photoproducing vector mesons and decaying to dark matter, thus rendering the secondary vector meson decay subdominant to dark bremsstrahlung. Since this counteraction is not seen to the same extent at electron beam experiments, it begs the question of why proton beam experiments suppress the photoproduction and vector meson decay relative to dark bremsstrahlung more strongly than electron beam experiments. Although no satisfactory reason was found in this thesis, possible explanations such as neglected photon production channels and to few high-energy photons were largely ruled out. This opens up

the question about the validity of the current modelling of dark bremsstrahlung production in proton and electron beam experiments. Interesting avenues for future work would therefore include the exploration of why this channel is suppressed for proton beam experiments, especially investigating the validity of current dark bremsstrahlung simulation tools. One strong contender is the overestimation of proton dark bremsstrahlung or the underestimation of electron dark bremsstrahlung production. Additional natural extensions include exploring other possible vector portal models, including other dark matter models or different mediators.

References

[1] J. J. Thomson, "Cathode Rays," *The London, Edinburgh, and Dublin Philosophical Magazine and Journal of Science*, vol. 44, no. 269, pp. 293–316, 1897. DOI: 10.1080/14786449708621070. eprint: https://doi.org/10.1080/14786449708621070. [Online]. Available: https://doi.org/10.1080/14786449708621070.

[2] E. Rutherford, "The scattering of alpha and beta particles by matter and the structure of the atom," *Phil. Mag. Ser. 6*, vol. 21, pp. 669–688, 1911. DOI: 10.1080/14786440508637080.

[3] N. Bohr, "On the constitution of atoms and molecules," *The London, Edinburgh, and Dublin Philosophical Magazine and Journal of Science*, vol. 26, no. 151, pp. 1–25, 1913. DOI: 10.1080/14786441308634955. eprint: https://doi.org/10.1080/14786441308634955. [Online]. Available: https://doi.org/10.1080/14786441308634955.

[4] Y. Nambu, "Particle physics in perspective," *Nuclear Physics A*, vol. 629, no. 1, pp. 3–8, 1998, Quark Lepton Nuclear Physics. DOI: https://doi.org/10.1016/S0375-9474(97)00659-3. [Online]. Available: https://www.sciencedirect.com/science/article/pii/S0375947497006593.

[5] G. Aad et al., "Observation of a new particle in the search for the Standard Model Higgs boson with the ATLAS detector at the LHC," *Physics Letters B*, vol. 716, no. 1, pp. 1–29, Sep. 2012. DOI: 10.1016/j.physletb.2012.08.020. [Online]. Available: http://dx.doi.org/10.1016/j.physletb.2012.08.020.

[6] M. Cirelli, A. Strumia, and J. Zupan, "Dark matter," *SciPost Phys. Rev.*, p. 1, 2026. DOI: 10.21468/SciPostPhysRev.1. [Online]. Available: https://scipost.org/10.21468/SciPostPhysRev.1.

[7] SHiP Collaboration, C. Ahdida, A. Akmete, and et al., "Sensitivity of the SHiP experiment to light dark matter," *J. High Energ. Phys.*, vol. 2021, no. 199, 2021. DOI: 10.1007/JHEP04(2021)199. [Online]. Available: https://doi.org/10.1007/JHEP04(2021)199.

[8] P. Schuster, N. Toro, and K. Zhou, "Probing invisible vector meson decays with the NA64 and LDMX experiments," *Physical Review D*, vol. 105, no. 3, Feb. 2022. DOI: 10.1103/physrevd.105.035036. [Online]. Available: http://dx.doi.org/10.1103/PhysRevD.105.035036.

[9] H. Katz, F. Lelli, S. S. McGaugh, A. Di Cintio, C. B. Brook, and J. M. Schombert, "Testing feedback-modified dark matter haloes with galaxy rotation curves: Estimation of halo parameters and consistency with ΛCDM scaling relations," *Monthly Notices of the Royal Astronomical Society*, vol. 466, no. 2, pp. 1648–1668, Apr. 2017. DOI: 10.1093/mnras/stw3101. eprint: https://academic.oup.com/mnras/article-pdf/466/2/1648/10867288/stw3101.pdf. [Online]. Available: https://doi.org/10.1093/mnras/stw3101.

[10] F. Zwicky, "On the Masses of Nebulae and of Clusters of Nebulae," *Astrophys. J.*, vol. 86, pp. 217–246, 1937. DOI: 10.1086/143864.

[11] A. R. Choudhuri, *Astrophysics for Physicists*. Cambridge University Press, 2010.

[12] N. Aghanim et al., "Planck 2018 results: VI. Cosmological parameters," *Astronomy & Astrophysics*, vol. 641, A6, Sep. 2020. DOI: 10.1051/0004-6361/201833910.

[13] G. Bertone and D. Hooper, "History of dark matter," *Rev. Mod. Phys.*, vol. 90, p. 045 002, 4 Oct. 2018. DOI: 10.1103/RevModPhys.90.045002. [Online]. Available: https://link.aps.org/doi/10.1103/RevModPhys.90.045002.

[14] J. D. Bjorken, R. Essig, P. Schuster, and N. Toro, "New fixed-target experiments to search for dark gauge forces," *Physical Review D*, vol. 80, no. 7, Oct. 2009. DOI: 10.1103/physrevd.80.075018. [Online]. Available: http://dx.doi.org/10.1103/PhysRevD.80.075018.

[15] M. Fabbrichesi, E. Gabrielli, and G. Lanfranchi, *The Physics of the Dark Photon: A Primer* (SpringerBriefs in Physics), 1st ed. Cham: Springer, 2021. DOI: 10.1007/978-3-030-62519-1. [Online]. Available: https://doi.org/10.1007/978-3-030-62519-1.

[16] O. Trivedi and R. J. Scherrer, "Dark Matter from Holography," Nov. 2025. arXiv: 2511.10617 [astro-ph.CO].

[17] G. Jungman, M. Kamionkowski, and K. Griest, "Supersymmetric dark matter," *Physics Reports*, vol. 267, no. 5, pp. 195–373, 1996. DOI: https://doi.org/10.1016/0370-1573(95)00058-5. [Online]. Available: https://www.sciencedirect.com/science/article/pii/0370157395000585.

[18] L. J. Hall, K. Jedamzik, J. March-Russell, et al., "Freeze-in production of FIMP dark matter," *J. High Energ. Phys.*, vol. 2010, p. 80, Mar. 2010. DOI: 10.1007/JHEP03(2010)080. [Online]. Available: https://doi.org/10.1007/JHEP03(2010)080.

[19] Y. Kahn and T. Lin, "Searches for light dark matter using condensed matter systems," *Reports on Progress in Physics*, vol. 85, no. 6, p. 066 901, May 2022. DOI: 10.1088/1361-6633/ac5f63. [Online]. Available: http://dx.doi.org/10.1088/1361-6633/ac5f63.

[20] A. Berlin, N. Blinov, G. Krnjaic, P. Schuster, and N. Toro, "Dark matter, millicharges, axion and scalar particles, gauge bosons, and other new physics with LDMX," *Physical Review D*, vol. 99, no. 7, Apr. 2019. DOI: 10.1103/physrevd.99.075001. [Online]. Available: http://dx.doi.org/10.1103/PhysRevD.99.075001.

[21] D. Tong, *The standard model*, University of Cambridge Part III Mathematical Tripos Lecture Notes. [Online]. Available: http://www.damtp.cam.ac.uk/user/tong/standardmodel.html.

[22] G. Krnjaic et al., "A Snowmass Whitepaper: Dark Matter Production at Intensity-Frontier Experiments," Jul. 2022. arXiv: 2207.00597 [hep-ph].

[23] R. Albanese et al., "BDF/SHiP Annual Report 2025," CERN, Geneva, Tech. Rep., 2025. [Online]. Available: https://cds.cern.ch/record/2948477.

[24] T. Zhou, R. Plestid, K. J. Kelly, et al., "Long-lived vectors from electromagnetic cascades at SHiP," *Journal of High Energy Physics*, vol. 2025, no. 2, p. 107, 2025. DOI: 10.1007/JHEP02(2025)107. [Online]. Available: https://doi.org/10.1007/JHEP02(2025)107.

[25] SHiP Collaboration and ECN3 Project Team, *SHiP experiment at the SPS Beam Dump Facility*, 2025. arXiv: 2504.06692 [hep-ex]. [Online]. Available: https://arxiv.org/abs/2504.06692.

[26] A. Betancur, A. Castillo, G. Palacio, and J. Suarez, "Multicomponent scalar dark matter at high-intensity proton beam experiments," *Journal of Physics G: Nuclear and Particle Physics*, vol. 49, no. 7, p. 075 003, Jun. 2022. DOI: 10.1088/1361-6471/ac65a6. [Online]. Available: https://doi.org/10.1088/1361-6471/ac65a6.

[27] V. Hewes et al., "Deep Underground Neutrino Experiment (DUNE) Near Detector Conceptual Design Report," *Instruments*, vol. 5, no. 4, p. 31, 2021. DOI: 10.3390/instruments5040031. arXiv: 2103.13910 [physics.ins-det].

[28] J. Sun et al., "Study of a hadron monitor for long baseline neutrino facility," *Nuclear Instruments and Methods in Physics Research Section A: Accelerators, Spectrometers, Detectors and Associated Equipment*, vol. 1027, p. 166 333, 2022. DOI: https://doi.org/10.1016/j.nima.2022.166333. [Online]. Available: https://www.sciencedirect.com/science/article/pii/S0168900222000225.

[29] V. Brdar et al., "Probing new physics at DUNE operating in a beam-dump mode," *Phys. Rev. D*, vol. 107, p. 055 043, 5 Mar. 2023. DOI: 10.1103/PhysRevD.107.055043. [Online]. Available: https://link.aps.org/doi/10.1103/PhysRevD.107.055043.

[30] L. Buonocore, C. Frugiuele, and P. deNiverville, "Hunt for sub-GeV dark matter at neutrino facilities: A survey of past and present experiments," *Physical Review D*, vol. 102, no. 3, Aug. 2020. DOI: 10.1103/physrevd.102.035006. [Online]. Available: http://dx.doi.org/10.1103/PhysRevD.102.035006.

[31] M. A. Acero et al., "First measurement of neutrino oscillation parameters using neutrinos and antineutrinos by NOvA," *Phys. Rev. Lett.*, vol. 123, p. 151 803, 15 Oct. 2019. DOI: 10.1103/PhysRevLett.123.151803. [Online]. Available: https://link.aps.org/doi/10.1103/PhysRevLett.123.151803.

[32] P. deNiverville and C. Frugiuele, "Hunting sub-gev dark matter with the NOνA near detector," *Phys. Rev. D*, vol. 99, 051701(R), 5 Mar. 2019. DOI: 10.1103/PhysRevD.99.051701. [Online]. Available: https://link.aps.org/doi/10.1103/PhysRevD.99.051701.

[33] S. Mufson et al., "Liquid scintillator production for the NOvA experiment," *Nuclear Instruments and Methods in Physics Research Section A: Accelerators, Spectrometers, Detectors and Associated Equipment*, vol. 799, pp. 1–9, 2015. DOI: https://doi.org/10.1016/j.nima.2015.07.026. [Online]. Available: https://www.sciencedirect.com/science/article/pii/S0168900215008554.

[34] A. Abed Abud, B. Abi, R. Acciarri, M. Acero, M. Adames, and T. D. collaboration, "DUNE Phase II: scientific opportunities, detector concepts, technological solutions," *Journal of Instrumentation*, vol. 19, no. 12, P12005, Dec. 2024. DOI: 10.1088/1748-0221/19/12/P12005. [Online]. Available: https://doi.org/10.1088/1748-0221/19/12/P12005.

[35] W. Jang, *Light dark matter search*, https://indico.cern.ch/event/1424413/contributions/6548794/attachments/3089921/5472111/NPN2025_06192025-wyjang.pdf, Presented at NPN 2025 (Cincinnati), June 19, 2025.

[36] V. De Romeri, K. J. Kelly, and P. A. Machado, "DUNE-PRISM sensitivity to light dark matter," *Physical Review D*, vol. 100, no. 9, Nov. 2019. DOI: 10.1103/physrevd.100.095010. [Online]. Available: http://dx.doi.org/10.1103/PhysRevD.100.095010.

[37] J. Bian, *Measurement of neutrino-electron elastic scattering at nova near detector*, 2017. arXiv: 1710.03428 [hep-ex]. [Online]. Available: https://arxiv.org/abs/1710.03428.

[38] L. Buonocore, C. Frugiuele, F. Maltoni, et al., "Event generation for beam dump experiments," *Journal of High Energy Physics*, vol. 2019, no. 5, p. 28, 2019. DOI: 10.1007/JHEP05(2019)028. [Online]. Available: https://doi.org/10.1007/JHEP05(2019)028.

[39] J. Alwall et al., "The automated computation of tree-level and next-to-leading order differential cross sections, and their matching to parton shower simulations," *Journal of High Energy Physics*, vol. 2014, no. 7, Jul. 2014. DOI: 10.1007/jhep07(2014)079. [Online]. Available: http://dx.doi.org/10.1007/JHEP07(2014)079.

[40] S. Navas et al., "Review of particle physics," *Phys. Rev. D*, vol. 110, no. 3, p. 030 001, 2024. DOI: 10.1103/PhysRevD.110.030001.

[41] C. Bierlich et al., *A comprehensive guide to the physics and usage of PYTHIA 8.3*, 2022. arXiv: 2203.11601 [hep-ph]. [Online]. Available: https://arxiv.org/abs/2203.11601.

[42] A. Segura and A. C. Parra, "A Practical Guide to Statistical Techniques in Particle Physics," Nov. 2024. arXiv: 2411.00706 [hep-ph].

[43] A. Lechner, "Particle interactions with matter," *CERN Yellow Rep. School Proc.*, vol. 5, B. Holzer, Ed., p. 47, 2018. DOI: 10.23730/CYRSP-2018-005.47.

[44] C. Ahdida, A. Akmete, R. Albanese, and A. Alexandrov, "Sensitivity of the SHiP experiment to dark photons decaying to a pair of charged particles," *The European Physical Journal C*, vol. 81, no. 5, May 2021. DOI: 10.1140/epjc/s10052-021-09224-3. [Online]. Available: http://dx.doi.org/10.1140/epjc/s10052-021-09224-3.

[45] CERN, *CERN Yellow Reports: Monographs, Vol 2 (2020): SPS Beam Dump Facility: Comprehensive Design Study*, 2020. DOI: 10.23731/CYRM-2020-002. [Online]. Available: https://e-publishing.cern.ch/index.php/CYRM/issue/view/106.

[46] S. Collaboration et al., *A facility to Search for Hidden Particles (SHiP) at the CERN SPS*, 2015. arXiv: 1504.04956 [physics.ins-det]. [Online]. Available: https://arxiv.org/abs/1504.04956.

[47] T. H. Bauer, R. D. Spital, D. R. Yennie, and F. M. Pipkin, "The hadronic properties of the photon in high-energy interactions," *Rev. Mod. Phys.*, vol. 50, pp. 261–436, 2 Apr. 1978. DOI: 10.1103/RevModPhys.50.261. [Online]. Available: https://link.aps.org/doi/10.1103/RevModPhys.50.261.

[48] I. S. Shapiro, "The optical model of the nucleus in the light of present-day data," *Phys. Usp.*, vol. 4, no. 5, pp. 674–697, 1962. DOI: 10.1070/PU1962v004n05ABEH003364. [Online]. Available: https://ufn.ru/en/articles/1962/5/b/.

[49] J.-M. Laget, "Photoproduction of vector mesons at large momentum transfer," *Physics Letters B*, vol. 489, no. 3–4, pp. 313–318, Sep. 2000. DOI: 10.1016/s0370-2693(00)00945-x. [Online]. Available: http://dx.doi.org/10.1016/S0370-2693(00)00945-X.

[50] P. deNiverville, C.-Y. Chen, M. Pospelov, and A. Ritz, "Light dark matter in neutrino beams: Production modeling and scattering signatures at MiniBooNE, T2K, and SHiP," *Physical Review D*, vol. 95, no. 3, Feb. 2017. DOI: 10.1103/physrevd.95.035006. [Online]. Available: http://dx.doi.org/10.1103/PhysRevD.95.035006.

[51] S. Balan et al., "Resonant or asymmetric: The status of sub-GeV dark matter," *Journal of Cosmology and Astroparticle Physics*, vol. 2025, no. 01, p. 053, Jan. 2025. DOI: 10.1088/1475-7516/2025/01/053. [Online]. Available: https://doi.org/10.1088/1475-7516/2025/01/053.

[52] P. deNiverville, M. Pospelov, and A. Ritz, "Observing a light dark matter beam with neutrino experiments," *Physical Review D*, vol. 84, no. 7, Oct. 2011. DOI: 10.1103/physrevd.84.075020. [Online]. Available: http://dx.doi.org/10.1103/PhysRevD.84.075020.

[53] I. Timiryasov, "Dark matter at the SHiP experiment," *EPJ Web Conf.*, vol. 125, V. A. Andrianov, V. A. Matveev, V. A. Rubakov, V. T. Kim, A. A. Andrianov, and M. D. Fitkevich, Eds., p. 02 023, 2016. DOI: 10.1051/epjconf/201612502023.

[54] K. J. Eskola, P. Paakkinen, H. Paukkunen, and C. A. Salgado, "Epps16: Nuclear parton distributions with lhc data," *The European Physical Journal C*, vol. 77, no. 3, Mar. 2017. DOI: 10.1140/epjc/s10052-017-4725-9. [Online]. Available: http://dx.doi.org/10.1140/epjc/s10052-017-4725-9.

[55] S. Dulat et al., "New parton distribution functions from a global analysis of quantum chromodynamics," *Physical Review D*, vol. 93, no. 3, Feb. 2016. DOI: 10.1103/physrevd.93.033006. [Online]. Available: http://dx.doi.org/10.1103/PhysRevD.93.033006.

[56] D. E. Soper, M. Spannowsky, C. J. Wallace, and T. M. Tait, "Scattering of dark particles with light mediators," *Physical Review D*, vol. 90, no. 11, Dec. 2014. DOI: 10.1103/physrevd.90.115005. [Online]. Available: http://dx.doi.org/10.1103/PhysRevD.90.115005.

[57] C. Anastasiou, L. Baudis, and V. Chiochia, *Phenomenology of particle physics i*, Lecture notes, ETH Zurich, 2010. [Online]. Available: https://edu.itp.phys.ethz.ch/hs10/ppp1/PPP1_2.pdf.

A

MadDump Code

Meson Decay Example

```
# Lengths in cm and masses in GeV
import model DM_mesons_2
import_events decay ....hepmc
decay pi0 > y1 a, y1 > xc xc~
define darkmatter xc
generate interaction @electron
output ...
set nb_core 20
launch
set flux_norm 6e20
set nevts_interaction 10000
set interpolation_method hist
set Z_average 44.
set A_average 106.
set prod_xsec_in_norm false
set d_target_detector 2500.00
set detector_density 7.08
set parallelepiped True
set x_side 40.0
set y_side 40.0
set depth 150
set ncores 8
set testplot True
set gvxd 0
set gvxc 2.242
set gvd11 -0.000100954
set gvu11 0.000201908
set gvd22 -0.000100954
set gvu22 0.000201908
set gvd33 -0.000100954
set gvu33 0.000201908
set gvl11 -0.000302862
set gvl22 -0.000302862
set gvl33 -0.000302862
set my1 scan1: [...]
set mxc scan1: [...]
set wy1 auto
set nfit 100k
```

```
set nexit 1k
```

Proton Bremsstrahlung Example

```
# Lengths in cm and masses in GeV
import model DM_mesons_2
define darkmatter xc
define bremsstrahlung y1
decay y1 > xc xc~
generate interaction @electron
output ...
set nb_core 20
launch
set nevts_interaction 10000
set interpolation_method hist
set Z_average 74.
set A_average 184.
set prod_xsec_in_norm false
set d_target_detector 2500.00
set detector_density 7.08
set parallelepiped True
set x_side 40.0
set y_side 40.0
set depth 150
set ncores 8
set testplot True
set gvxd 0.
set gvxc 2.242
set gvd11 -0.000100954
set gvu11 0.000201908
set gvd22 -0.000100954
set gvu22 0.000201908
set gvd33 -0.000100954
set gvu33 0.000201908
set gvl11 -0.000302862
set gvl22 -0.000302862
set gvl33 -0.000302862
set my1 scan1: [...]
set mxc scan1: [...]
set wy1 auto
# bremsstrahlung paramaters
set npot 6e20
set pbeam 400.
set ngen 100k
set z_min 0.1
set z_max 0.9
set pt2_max 16.
# paramaters of the fit
set nfit 100k
set nexit 1k
```

B

Pythia Code

Meson

```
#include "Pythia8/Pythia.h"
#include "Pythia8Plugins/HepMC2.h"
#include <set>

using namespace Pythia8;
int main() {
        Pythia pythia;

        // Mesons to keep
        std::set<int> keepMesons = {
                    111,  // pi0
                    221,  // eta
                    223,  // omega
        };

        // Define new particle
        pythia.particleData.addParticle(1000741840, "184W", 1,
        222, 0, 171.3492094385);

        // Store events
        Pythia8ToHepMC toHepMC("....hepmc");

        pythia.readString("Beams:idA = 2212"); // Proton has PDG code 2212
        pythia.readString("Beams:idB = 1000741840"); // New W particle

        // Run fixed target (frametype 2, beam B particles at rest).
        pythia.readString("Beams:eA = 400");
        pythia.readString("Beams:eB = 0");
        pythia.readString("Beams:frameType = 2");
        pythia.readString("HeavyIon:SigFitNGen = 40");
        pythia.readString("SoftQCD:inelastic = on");

        // When on, only particles with tau0 < tau0Max are decayed.
        pythia.readString("ParticleDecays:limitTau0 = on");
        pythia.readString("ParticleDecays:tau0Max = 0");

        // Prevent selected mesons from decaying
        for (int id : keepMesons) {
        pythia.readString(std::to_string(id) + ":mayDecay = off");
```

```
        }

        // The number of events to be generated.
        pythia.readString("Main:numberOfEvents = 100000");

        // If Pythia fails to initialize, exit with error.
        if (!pythia.init()) return 1;

        // Event loop
        for (int iEvent = 0; iEvent < pythia.mode("Main:numberOfEvents");
        ++iEvent) {
            if (!pythia.next()) continue;

            // Original event size and event size after filtering
            int sizeNew = 3;

            // Remove all particles except the ones in 'keepMesons'
            for (int i = 3; i < pythia.event.size(); ++i) {
            Particle& p = pythia.event[i];

                if (keepMesons.count(p.id())) {

                    pythia.event[sizeNew] = pythia.event[i];

                    // Particles should have mothers, so select beam particles.
                    pythia.event[sizeNew].mothers(1,2);

                    // Make sure particle has no daughters
                    pythia.event[sizeNew].daughters(0,0);
                    ++sizeNew;
                }
            }

            // Remove the ones that did not pass the checks
            pythia.event.popBack( pythia.event.size() - sizeNew);

            // Beam particles should have remaining particles as daughters.
            pythia.event[1].daughters( 3, sizeNew - 1);
            pythia.event[2].daughters( 3, sizeNew - 1);

        // List first compressed event.
        if (iEvent == 0) pythia.event.list();

        // Convert and write the modified event to HepMC
        toHepMC.writeNextEvent(pythia);
    }

    // Print statistics
    pythia.stat();

    // Done.
    return 0;
}
```

Photon

```
#include "Pythia8/Pythia.h"
#include "Pythia8Plugins/HepMC2.h"

using namespace Pythia8;

int main() {
    Pythia pythia;

    // Add Molybdenum (96Mo)
    pythia.particleData.addParticle(
        1000420960, "96Mo", 1, 126, 0, 89.334638710673857
    );

    // Output file
    Pythia8ToHepMC toHepMC("....hepmc");

    // Create beams
    pythia.readString("Beams:idA=2212"); // Proton (PDG code=2212) beam
    pythia.readString("Beams:idB=1000420960"); // New Mo particle

    // Run fixed target
    pythia.readString("Beams:eA = 400");
    pythia.readString("Beams:eB = 0");
    pythia.readString("Beams:frameType = 2");

    // Switched on processes
    pythia.readString("SoftQCD:inelastic = on"); // Meson decay channel

    // Decays
    pythia.readString("HeavyIon:SigFitNGen = 40");
    pythia.readString("HadronLevel:Decay = on");

    // Number of events
    pythia.readString("Main:numberOfEvents = 10000");

    // Fail safe
    if (!pythia.init()) return 1;

    // Event loop
    for (int iEvent = 0; iEvent < pythia.mode("Main:numberOfEvents");++iEvent){
        if (!pythia.next()) continue;
        if (iEvent == 0) pythia.event.list();
        toHepMC.writeNextEvent(pythia);
    }

    pythia.stat();
    return 0;
}
```

C

Complex Scalar DM Decay Rate

The Feynman amplitude for an on-shell vector meson with four-momentum q^μ decaying into on-shell complex scalar dark matter χ and its antiparticle $\chi^\dagger$ with four-momenta p^μ and p'^μ respectively is

$$\mathcal{M} = \epsilon e m_V f_V \epsilon_\mu \frac{\eta^{\mu\nu} - q^\mu q^\nu / m_{A'}^2}{q^2 - m_{A'}^2} g_D (p - p')_\nu. \tag{C.1}$$

The second term in the propagator vanishes due to the on-shell conditions of the final-state particles. Using four-momentum conservation $q^\mu = p^\mu + p'^\mu$, this is easily seen

$$q^\nu (p - p')_\nu = (p + p')^\nu (p - p')_\nu = p^2 - p'^2 = m_\chi^2 - m_\chi^2 = 0. \tag{C.2}$$

The amplitude therefore reduces to

$$\mathcal{M} = \frac{g_D \epsilon e m_V f_V}{q^2 - m_{A'}^2} \epsilon^\nu (p - p')_\nu \equiv C \epsilon^\nu (p - p')_\nu. \tag{C.3}$$

Squaring and averaging over the initial meson polarisations, noting that a massive vector meson has three degrees of freedom, gives

$$\begin{aligned} |\overline{\mathcal{M}}|^2 &= |C|^2 (p - p')_\nu (p - p')_\mu \frac{1}{3} \sum_{\text{pol}} \epsilon^\nu \epsilon^{*\mu} \\ &= \frac{|C|^2}{3} (p - p')_\nu (p - p')_\mu \left(-\eta^{\mu\nu} + \frac{q^\mu q^\nu}{m_V^2} \right) \\ &= -\frac{|C|^2}{3} (p - p')^2 = -\frac{|C|^2}{3} (p^2 + p'^2 - 2p \cdot p') \\ &= -\frac{|C|^2}{3} (m_\chi^2 + m_\chi^2 - (m_V^2 - 2m_\chi^2)) = \frac{|C|^2}{3} (m_V^2 - 4m_\chi^2), \end{aligned} \tag{C.4}$$

using $m_V^2 = q^2 = p^2 + p'^2 + 2p \cdot p' = 2m_\chi^2 + 2p \cdot p'$ such that $2p \cdot p' = (m_V^2 - 2m_\chi^2)$. The term $q^\mu q^\nu$ vanishes upon contraction by the same argument as before

$$(p - p')_\nu (p - p')_\mu q^\nu q^\mu = [q^\nu (p - p')_\nu]^2 = 0. \tag{C.5}$$

Once the squared Feynman amplitude is determined, the next step is to compute the decay rate given by

$$\Gamma = \frac{1}{2m_V} |\overline{\mathcal{M}}|^2 \int d\text{Lips}_2 \tag{C.6}$$

In the rest frame of the vector meson, the two-body Lorentz-invariant phase space integral evaluates to

$$\begin{aligned}\int d\text{Lips}_2 &= \int \delta^{(4)}(q^\mu - p^\mu - p'^\mu)(2\pi)^4 \frac{d^3\vec{p}}{(2\pi)^3 2E_p}\frac{d^3\vec{p}'}{(2\pi)^3 2E'_p} \\ &= \frac{1}{4(2\pi)^2}\int \delta(m_V - E_p - E_{p'})\delta^{(3)}(\vec{p}+\vec{p}')\frac{d^3\vec{p}}{E_p}\frac{d^3\vec{p}'}{E_{p'}} \\ &= \frac{1}{4(2\pi)^2}\int \delta(m_V - 2E_p)(4\pi p^2)\frac{dp}{E_p^2}.\end{aligned} \tag{C.7}$$

Performing the change of variables $E_p^2 = p^2 + m_\chi^2 \implies dE_p = pdp/E_p$ gives

$$\begin{aligned}\int d\text{Lips}_2 &= \frac{1}{4\pi}\int \delta(m_V - 2E_p)\frac{p}{E_p}dE_p \\ &= \frac{1}{4\pi}\int \frac{1}{2}\delta(E_p - m_V/2)\frac{\sqrt{E_p^2 - m_\chi^2}}{E_p}dE_p \\ &= \frac{1}{8\pi}\frac{\sqrt{(m_V/2)^2 - m_\chi^2}}{(m_V/2)} = \frac{1}{8\pi m_V}\sqrt{m_V^2 - 4m_\chi^2}.\end{aligned} \tag{C.8}$$

Substituting everything into equation (C.6) yields

$$\begin{aligned}\Gamma &= \frac{1}{2m_V}\frac{|C|^2}{3}(m_V^2 - 4m_\chi^2)\frac{1}{8\pi m_V}\sqrt{m_V^2 - 4m_\chi^2} = \frac{|C|^2}{48\pi m_V^2}(m_V^2 - 4m_\chi^2)^{3/2} \\ &= \frac{1}{48\pi}\left|\frac{g_D\epsilon e m_V f_V}{q^2 - m_{A'}^2}\right|^2 (m_V^2 - 4m_\chi^2)^{3/2}.\end{aligned} \tag{C.9}$$

To account for the resonant peak, the propagator is dressed by including higher-order self-energy insertions

$$\begin{aligned}\frac{1}{q^2 - m_{A'}^2} &\to \frac{1}{q^2 - m_{A'}^2} + \frac{1}{q^2 - m_{A'}^2}\Pi(q^2)\frac{1}{q^2 - m_{A'}^2} + \dots \\ &\simeq \frac{1}{m_V^2 - m_{A'}^2 - i m_{A'}\Gamma_{A'}}.\end{aligned} \tag{C.10}$$

where $\Gamma_{A'}$ is the decay rate for an on-shell A' into dark matter. It can be computed similarly. Its Feynman amplitude is $\mathcal{M} = \epsilon_\mu g_D (p - p')^\mu$. Taking the square and averaging over initial meson polarisations, the steps are the same as before, leading to

$$|\overline{\mathcal{M}}|^2 = \frac{g_D^2}{3}(m_{A'}^2 - 4m_\chi^2). \tag{C.11}$$

The two-body Lorentz invariant phase space integral has already been computed. Replacing m_V with $m_{A'}$ in equations (C.6) and (C.8), one finds

$$\Gamma_{A'} = m_{A'}\frac{\alpha_D}{12}\left(1 - \frac{4m_\chi^2}{m_{A'}^2}\right)^{3/2}. \tag{C.12}$$

The final result for the complex scalar dark matter decay rate is thus

$$\Gamma(V \to \chi\bar{\chi}) = \frac{\alpha_D(\epsilon e)^2 f_V^2}{12}\frac{(m_V^2 - 4m_\chi^2)^{3/2}}{(m_{A'}^2 - m_V^2)^2 + m_{A'}^2\Gamma_{A'}^2}, \tag{C.13}$$

D

Elastic Two-Body Scattering

This appendix presents the derivation of the kinematically allowed region for a two-body scattering process used when computing cross sections for the dark matter detection in section 4.4. It closely follows the logic outlined in the lecture notes [57].

Consider a general two-body scattering process $X_1(p_1) + X_2(p_2) \to X_3(p_3) + X_4(p_4)$ illustrated in figure D.1. The Mandelstam variables are Lorentz invariant quantities encoding the four-momenta of the process. They are defined as

$$\begin{aligned} s &= (p_1 + p_2)^2 = (p_3 + p_4)^2 \\ t &= (p_1 - p_3)^2 = (p_2 - p_4)^2 \\ u &= (p_1 - p_4)^2 = (p_2 - p_3)^2, \end{aligned} \tag{D.1}$$

and it is easily shown that $s + t + u = m_1^2 + m_2^2 + m_3^2 + m_4^2$. Naturally, the constraints of the process are energy–momentum conservation and the on-shell condition

$$p_1 + p_2 = p_3 + p_4, \qquad p_i^2 = m_i^2, \quad i \in \{1, 2, 3, 4\}. \tag{D.2}$$

The process may be viewed from the centre-of-mass frame, such that

$$\vec{p} \equiv \vec{p}_1^{\,*} = -\vec{p}_2^{\,*}, \qquad \vec{p}\,' \equiv \vec{p}_3^{\,*} = -\vec{p}_4^{\,*}. \tag{D.3}$$

Here, an asterisk is used to denote variables in the centre-of-mass frame. Using the above relations, the energy E_i and magnitude of the momentum $|\vec{p}|$ can be expressed

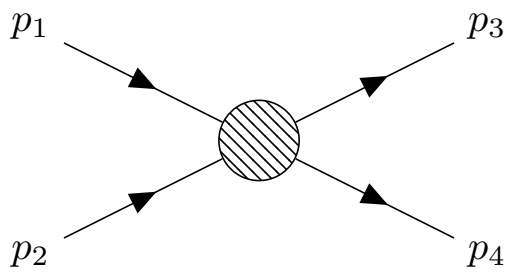

Figure D.1: Illustration of a generic two-body scattering process.

in terms of s

$$E^*_{1,3} = \frac{s + m^2_{1,3} - m^2_{2,4}}{2\sqrt{s}}, \qquad |\vec{p}|^2 = \frac{\lambda(s, m_1^2, m_2^2)}{4s}, \tag{D.4}$$

where λ is the Källén (triangle) function, defined as

$$\lambda(a, b, c) \equiv a^2 - 2a(b + c) + (b - c)^2. \tag{D.5}$$

Furthermore, the scattering angle θ^* is the angle between $\vec{p}$ and $\vec{p}\,'$ and can be shown to equal

$$\cos\theta^* \equiv \frac{\vec{p}\cdot\vec{p}\,'}{|\vec{p}||\vec{p}\,'|} = \frac{s(t-u) + (m_1^2 - m_2^2)(m_3^2 - m_4^2)}{\sqrt{\lambda(s, m_1^2, m_2^3)}\sqrt{\lambda(s, m_3^2, m_4^2)}}. \tag{D.6}$$

The two-body process has two degrees of freedom and can therefore be fully specified by either $\sqrt{s}$ and θ^*, or by $\sqrt{s}$ and t.

Restricting the rest of the discussion to elastic two-body scattering, the initial and final particles are the same: $X \equiv X_1 = X_3$ and $Y \equiv X_2 = X_4$. Consequently, $m_1 = m_3$ and $m_2 = m_4$, and equation (D.4) now reduces to

$$E_1^* = E_3^*, \qquad E_2^* = E_4^*, \qquad |\vec{p}|^2 = |\vec{p}\,'|^2 = \frac{1}{4s}(s - [m_1 + m_2]^2)(s - [m_1 - m_2]^2). \tag{D.7}$$

It can then be noticed that

$$t = (p_1 - p_3)^2 = -(\vec{p}_1 - \vec{p}_3)^2 = -2|\vec{p}|^2(1 - \cos\theta^*). \tag{D.8}$$

The physical region is restricted by $|\vec{p}|^2 \geq 0$ and $-1 \leq \cos\theta^* \leq 1$, which by observing equation (D.7) as well as (D.8), together with equation (D.4), implies

$$-4|\vec{p}|^2 = -\frac{\lambda(s, m_1^2, m_2^2)}{s} \leq t \leq 0, \qquad (m_1 + m_2)^2 \leq s. \tag{D.9}$$

Having expressed the kinematically allowed region in Lorentz-invariant form, one may switch to the laboratory frame. Then X is the projectile particle, whose initial state is denoted X_1 and recoil final state X_3, and Y is the target particle whose initial state is X_2 and recoil final state is X_4, such that $p_2 = (m_2, \vec{0})$. The s Mandelstam variable is then easily identified as $s = (p_1 + p_2)^2 = m_1^2 + m_2^2 + 2E_1 m_2$. Consequently, $\lambda(s, m_1^2, m_2^2) = 4m_2^2(E_1^2 - m_2^2)$. Finally, $t = (p_2 - p_4)^2 = 2m_2(E_3 - E_1)$ using energy conservation $E_1 + m_2 = E_3 + E_4$. Thus, in the laboratory frame, the right-hand side states $m_1 \leq E_1$, while the left-hand side can either be stated in terms of the recoiled target particle X_4

$$0 \leq E_4 \leq m_2 + \frac{2m_2(E_1^2 - m_1^2)}{m_1^2 + m_2^2 + 2E_1 m_2}. \tag{D.10}$$

or, alternatively, in terms of the recoiled projectile particle X_3

$$E_1 - \frac{2m_2(E_1^2 - m_1^2)}{m_1^2 + m_2^2 + 2E_1 m_2} \leq E_3 \leq E_1. \tag{D.11}$$

If one requires the recoil target particle energy E_4 to have a certain minimum value $E_4 > E_{\text{cut}}$, then the left-hand side of equation (D.10) is modified to E_{cut} and the right-hand side of equation (D.11) is modified to $E_1 + m_2 - E_{\text{cut}}$.

E

Deep Inelastic Scattering

In this appendix, the differential cross section for the deep inelastic scattering of a complex dark matter particle χ from a nucleus N is calculated. Denote the incoming (outgoing) dark matter momentum p (p'), and the momentum of the nucleus with P. In the rest frame of the nucleus, $P = (M, \vec{0})$, $p = (E, \vec{p})$ and $p' = (E', \vec{p}')$. The scattering occurs through en exchange of a virtual dark photon A' with four-momentum $q = p - p' = (\nu, \vec{q})$ in the nucleus rest frame. Useful relations include

$$P \cdot q = M\nu, \qquad P \cdot p = ME, \qquad p \cdot q = -\frac{Q^2}{2}, \tag{E.1}$$

defining $Q^2 = -q^2$ such that $Q > 0$. The on-shell relation also dictates $p^2 = p'^2 = m_\chi^2$ and $P^2 = M^2$. The Feynman diagram of the scattering process is depicted in figure 3.5b. From it, the Feynman amplitude can easily be deduced. The dark matter vertex contributes with $g_D(p + p')^\mu$ and the virtual dark photon with the usual massive $-i(\eta^{\mu\nu} - q^\mu q^\nu / m_{A'}^2)/(q^2 - m_{A'}^2)$. In the lowest order perturbation of the interaction, the nucleus contribution is regarded with a form factor defined by the matrix element $f^\nu = \sum_X \langle X|J^\nu(0)|P\rangle$, where J_μ is the electromagnetic current $J^\mu = \sum_q Q_q \bar{q}\gamma^\mu q$. This vertex describes the interaction between the quarks and the dark photon, and therefore contribute with the coupling strength $(e\epsilon)$. All in all, the Feynman amplitude is

$$\mathcal{M} = \frac{(e\epsilon)g_D}{q^2 - m_{A'}^2}\left(-\eta_{\mu\nu} + \frac{q_\mu q_\nu}{m_{A'}^2}\right)(p + p')^\mu f^\nu \tag{E.2}$$

Conservation of electromagnetism enforces $q_\nu f^\nu$, such that the second term in the propagator vanishes. Squaring the amplitude gives

$$|\overline{\mathcal{M}}|^2 = \frac{(e\epsilon)^2 \alpha_D^2}{(q^2 - m_{A'}^2)^2} L_{\mu\nu} f^\mu f^\nu, \tag{E.3}$$

defining $L_{\mu\nu} = (p+p')_\mu (p+p')_\nu$. The differential cross section is then given by

$$\begin{aligned} d\sigma &= \frac{1}{4\sqrt{(p\cdot P)^2 - m_\chi^2 M^2}} |\overline{\mathcal{M}}|^2 d\text{Lips} \\ &= \frac{(e\epsilon)^2 \alpha_D^2}{4M\sqrt{E^2 - m_\chi^2}} \frac{L_{\mu\nu} f^\mu f^\nu}{(q^2 - m_{A'}^2)^2} (2\pi)^4 \delta^{(4)}(p + P - p' - p_X) \frac{d^3p'}{(2\pi)^3 2E'} \\ &= \frac{\pi (e\epsilon)^2 g_D^2}{8\pi^2 M\sqrt{E^2 - m_\chi^2}} \frac{L_{\mu\nu} W^{\mu\nu}}{(q^2 - m_{A'}^2)^2} \frac{d^3p'}{2E'}, \end{aligned} \tag{E.4}$$

where $1/(4\sqrt{(p\cdot P)^2 - m_\chi^2 M^2})$ is the flux, simplified using the relation in equation (E.1). dLips is the Lorentz invariant phase space measure and the hadronic matrix element describing the quark current has been introduced with its conventional factor $(4\pi)^{-1}$ as

$$W_{\mu\nu} \equiv \frac{1}{4\pi} (2\pi)^4 \delta^{(4)}(P + q - p_X) \sum_X \langle P|J_\mu(0)|X\rangle \langle X|J_\nu(0)|P\rangle . \tag{E.5}$$

The differential cross section may be rewritten in more convenient integration variables $d^3p' \to d\nu dQ^2$

$$\frac{d^3p'}{2E'} = \frac{2\pi p'^2}{2E'} d(\cos\theta) dp' = \frac{2\pi p'^2}{2E'} \left| \frac{\partial(p', \cos\theta)}{\partial(\nu, Q^2)} \right| d\nu dQ^2 = \frac{\pi}{2\sqrt{E^2 - m_\chi^2}} d\nu dQ^2, \tag{E.6}$$

computing the Jacobian using the following relations

$$\begin{aligned} E'^2 &= (E-\nu)^2 = p'^2 + m_\chi^2, \\ Q^2 &= -q^2 = -(p-p')^2 = 2E(E-\nu) - 2pp'\cos\theta - 2m_\chi^2, \\ p &= \sqrt{E^2 - m_\chi^2}. \end{aligned} \tag{E.7}$$

Performing the change in variables results in

$$d\sigma = \frac{(e\epsilon)^2 g_D^2}{16\pi M} \frac{d\nu dQ^2}{E^2 - m_\chi^2} \frac{L_{\mu\nu} W^{\mu\nu}}{(q^2 - m_{A'}^2)^2}. \tag{E.8}$$

Following [56], the hadronic matrix element may be expressed in its standard structure functions

$$W_{\mu\nu} = C_T^{\mu\nu} F_T(x_{\text{bj}}, Q^2) + C_L^{\mu\nu} F_L(x_{\text{bj}}, Q^2). \tag{E.9}$$

where C_L and C_T correspond to the exchange of a longitudinal and transverse polarised virtual vector mediator respectively. The structure functions F_L and F_T can be expressed as a convolution of the parton distribution functions with the partonic structure functions $\hat{F}_L$ and $\hat{F}_T$. At lowest order, both of these vanishes for the gluon, whilst the former vanishes for quarks. Only $\hat{F}_T$ remains, which takes the form of a delta function, imposing the parton fraction momentum x to take the value of the Bjorken scaling variable

$$x_{\text{bj}} \equiv \frac{Q^2}{2M\nu}. \tag{E.10}$$

Consequently, the structure functions take the form

$$F_L = 0, \qquad F_T = \frac{1}{2x_{\mathrm{bj}}} \sum_q x_{\mathrm{bj}} f_{q/A}(x_{\mathrm{bj}}, Q^2). \tag{E.11}$$

The reason for multiplying and dividing with x_{bj} is that the parton distribution function $f_{q/A}(x)$ is ill-behaved close to zero. The cross section is therefore

$$d\sigma = \frac{(e\epsilon)^2 g_D^2}{16\pi M} \frac{d\nu dQ^2}{E^2 - m_\chi^2} \frac{L_{\mu\nu} C_T^{\mu\nu}}{(q^2 - m_{A'}^2)^2} \frac{1}{2x_{\mathrm{bj}}} \sum x_{\mathrm{bj}} f_{q/A}(x_{\mathrm{bj}}, Q^2), \tag{E.12}$$

The $C_T^{\mu\nu}$ is explicitly expressed as

$$C_T^{\mu\nu} = -\eta^{\mu\nu} + \frac{q^\mu q^\nu}{q^2} + \frac{2x_{\mathrm{bj}}}{P \cdot q + 2x_{\mathrm{bj}} M^2} \left(P^\mu + \frac{P \cdot q}{q^2} q^\mu \right) \left(P^\nu + \frac{P \cdot q}{q^2} q^\nu \right). \tag{E.13}$$

Using the relations in equation (E.1) the contraction between it and $L_{\mu\nu}$ is computed to be

$$L_{\mu\nu} C_T^{\mu\nu} = \frac{Q^2}{\nu^2 + Q^2} (2E - \nu)^2 - Q^2 - 4m_\chi^2. \tag{E.14}$$

Putting everything together, the final expression for the deep inelastic scattering is hence

$$\frac{d\sigma}{d\nu dQ^2} = \frac{\pi \epsilon^2 \alpha_D \alpha}{E^2 - m_\chi^2} \frac{\nu}{(Q^2 - m_{A'}^2)^2} \left[\frac{(E - \nu)^2}{\nu^2 + Q^2} - \frac{Q^2 + 4m_\chi^2}{Q^2} \right] \sum x_{\mathrm{bj}} f_{q/A}(x_{\mathrm{bj}}, Q^2). \tag{E.15}$$

DEPARTMENT OF PHYSICS AND ASTRONOMY
CHALMERS UNIVERSITY OF TECHNOLOGY
Gothenburg, Sweden
www.chalmers.se

CHALMERS
UNIVERSITY OF TECHNOLOGY